

RESEARCH ARTICLE

Contractility kits promote assembly of the mechanoresponsive cytoskeletal network

Priyanka Kothari¹, Vasudha Srivastava^{1,2,*}, Vasudha Aggarwal^{3,‡}, Irina Tchernyshyov⁴, Jennifer E. Van Eyk⁴, Taekjip Ha^{3,5,6,7} and Douglas N. Robinson^{1,2,8,9,§}

ABSTRACT

Cellular contractility is governed by a control system of proteins that integrates internal and external cues to drive diverse shape change processes. This contractility controller includes myosin II motors, actin crosslinkers and protein scaffolds, which exhibit robust and cooperative mechanoaccumulation. However, the biochemical interactions and feedback mechanisms that drive the controller remain unknown. Here, we use a proteomics approach to identify direct interactors of two key nodes of the contractility controller in the social amoeba *Dictyostelium discoideum*: the actin crosslinker cortexillin I and the scaffolding protein IQGAP2. We highlight several unexpected proteins that suggest feedback from metabolic and RNA-binding proteins on the contractility controller. Quantitative *in vivo* biochemical measurements reveal direct interactions between myosin II and cortexillin I, which form the core mechanosensor. Furthermore, IQGAP1 negatively regulates mechanoresponsiveness by competing with IQGAP2 for binding the myosin II–cortexillin I complex. These myosin II–cortexillin I–IQGAP2 complexes are pre-assembled into higher-order mechanoresponsive contractility kits (MCKs) that are poised to integrate into the cortex upon diffusional encounter coincident with mechanical inputs.

This article has an associated First Person interview with the first author of the paper.

KEY WORDS: Myosin II, Cortexillin I, IQGAP, LC-MS, FCCS, SiMPull

INTRODUCTION

Every biological process is dependent upon the ability of a cell to sense and adapt to its dynamic environment. As a result, control systems with sensors, modulators and feedback loops have evolved to govern cellular processes ranging from metabolism to cell cycle regulation (Umbarger, 1956; Ferrell, 2013). Macromolecules

modulate their behavior in response to internal and external cues, and regulatory proteins integrate those cues through feedback loops to further tune the response of the cell. Cellular contractility is a prime example of such a control system, as it is driven by molecular machinery that is spatially and temporally regulated by feedback loops (Effler et al., 2006; Ren et al., 2009; Luo et al., 2012, 2013; Schiffhauer et al., 2016) (Fig. 1A). For example, during cell migration, chemical cues drive actin polymerization at the leading edge, resulting in tension in the cortical network that causes the contractile machinery to accumulate at the lagging edge, thereby allowing the cell to move forward (Lee et al., 2010). Similarly, mitotic spindle signals coordinate the initial accumulation of mechanoresponsive proteins to the furrow during cytokinesis, and resulting stresses tune the amount of protein required to drive cleavage furrow ingression (Kee et al., 2012; Srivastava and Robinson, 2015). We define this integrated network of macromolecules that allows cells to generate, sense and respond to forces in different processes as the mechanobiome.

The mechanoenzyme non-muscle myosin II is a critical component of the mechanobiome as it can stiffen the cell cortex and generate contractile force, but can also modulate the assembly and disassembly dynamics and fluid characteristics of the network (Girard et al., 2006; Poirier et al., 2012; Srivastava and Robinson, 2015). Although myosin II is evolutionarily conserved from the social amoeba *Dictyostelium discoideum* to higher metazoans, under certain conditions, cells can complete cytokinesis in the absence of myosin II (De Lozanne and Spudich, 1987; Kanada et al., 2005). Thus, an integrated cortical network still exists in the absence of myosin II, and this network is able to generate force and cortical tension, providing active forces and Laplace pressure-mediated furrow thinning that can drive cytokinesis (Zhang and Robinson, 2005; Poirier et al., 2012).

While myosin II is the force-generating arm, the dimeric actin crosslinker cortexillin I acts as the force-bearing component of the *Dictyostelium* contractile machinery (Ren et al., 2009; Luo et al., 2012). Cortexillin I anchors the cortical cytoskeletal network to the membrane through its actin-binding and lipid-binding domains (Faix et al., 2001). Genetic dissection demonstrates that myosin II and cortexillin I require each other for their mechanoresponsiveness, and their mechanoresponsive behavior is regulated by the cortexillin I-binding scaffolding IQGAP proteins (Fig. 1A) (Ren et al., 2009; Luo et al., 2012). IQGAP1 inhibits the mechanoresponsive accumulation of myosin II and cortexillin I, while IQGAP2 relieves this repression (Kee et al., 2012; Faix and Weber, 2013; Ren et al., 2014; Srivastava and Robinson, 2015). In addition, *iqg1* (encoding IQGAP1)-null *Dictyostelium* cells migrate faster than wild-type, providing further evidence for IQGAP1 as a negative regulator of contractility (Lee et al., 2010). These IQGAP feedback loops actively tune the levels of accumulation of contractile machinery at sites of mechanical stress. During cytokinesis, for example, IQGAP2 recruits mitotic signaling proteins, including kinesin 6 (kif12 in *Dictyostelium*) and INCENP,

¹Department of Cell Biology, Johns Hopkins University School of Medicine, Baltimore, MD 21205, USA. ²Department of Chemical and Biomolecular Engineering, Johns Hopkins University, Baltimore, MD 21218, USA. ³Department of Biophysics and Biophysical Chemistry, Johns Hopkins University School of Medicine, Baltimore, MD 21205, USA. ⁴Department of Medicine, The Smidt Heart Institute and Advanced Clinical Biosystems Institute, Cedar-Sinai Medical Center, Los Angeles, CA 90048, USA. ⁵Department of Biophysics, Johns Hopkins University, Baltimore, MD 21218, USA. ⁶Department of Biomedical Engineering, Johns Hopkins University, Baltimore, MD 21205, USA. ⁷Howard Hughes Medical Institute, Baltimore, MD 21205, USA. ⁸Department of Pharmacology and Molecular Sciences, Johns Hopkins University School of Medicine, Baltimore, MD 21205, USA. ⁹Department of Medicine, Johns Hopkins University School of Medicine, Baltimore, MD 21205, USA.

*Present address: Department of Pharmaceutical Chemistry, University of California San Francisco, San Francisco, CA 94158, USA. ‡Present address: Quantapore Inc, Menlo Park, CA 94025, USA.

§Author for correspondence (dnr@jhmi.edu)

© V.A., 0000-0001-9856-1292; D.N.R., 0000-0003-1236-4891

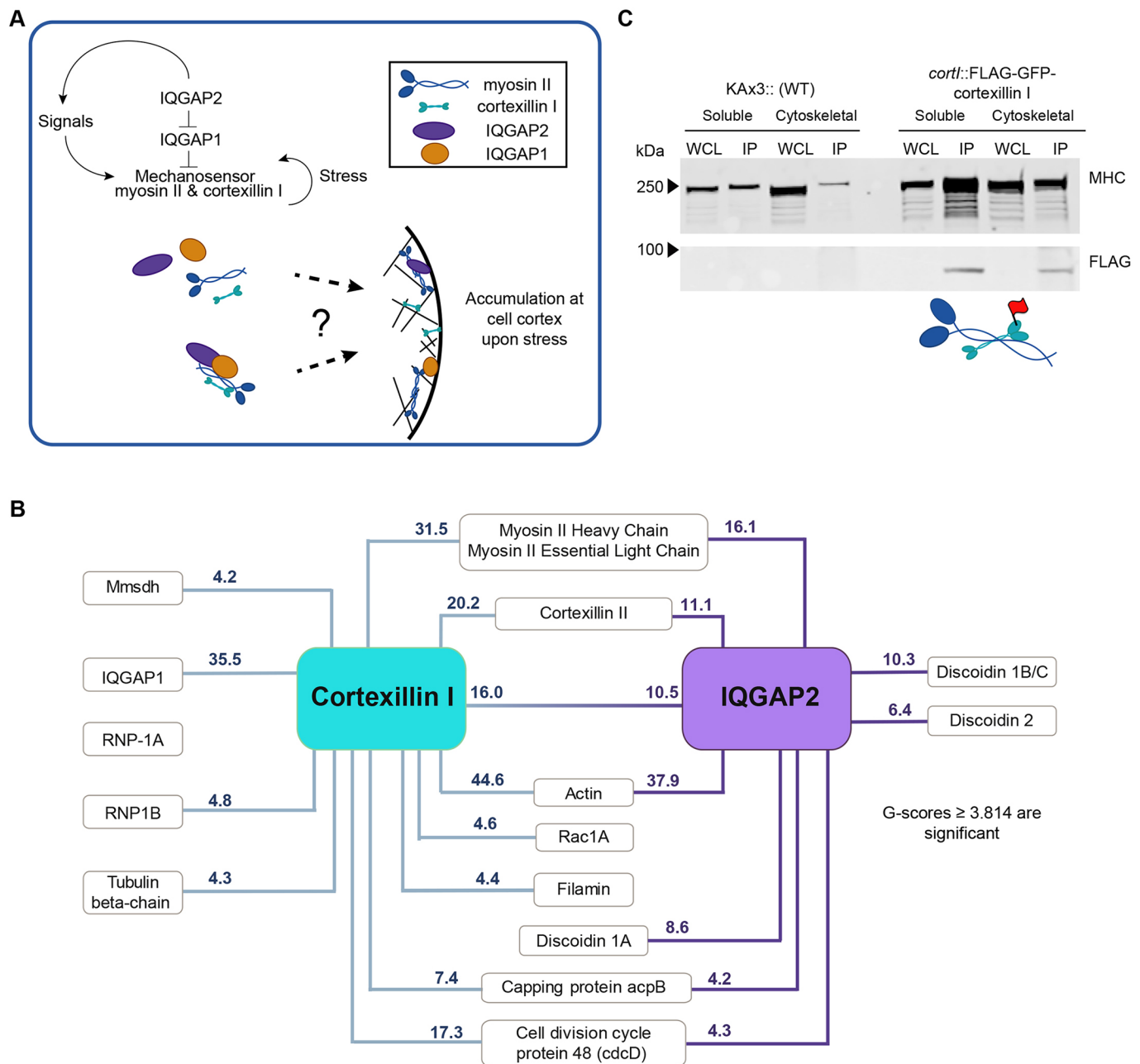


Fig. 1. Identification of protein interactors of the contractility control system by mass spectrometry and immunoprecipitation. (A) A schematic of the core contractility controller that governs assembly of contractile machinery (myosin II and cortexillin I). Chemical and mechanical signals, as well as feedback through the IQGAPs, tune the accumulation of contractile machinery at the site of stress. Whether these proteins accumulated individually or through pre-assembled complexes under stress was unknown. (B) Potential protein interactions identified by cytoskeletal fractionation and immunoprecipitation followed by LC-MS. Lines between proteins indicate potential interactions, with corresponding G-scores from comparison with GFP control for cytosolic or cytoskeletal fractions. RNP-1A was not detected by mass spectrometry, but is related to RNP-1B and was discovered as a genetic suppressor of nocodazole. Results are from three biological replicates. (C) Precipitation of FLAG-GFP from KAx3 (WT) or *cortI::FLAG-GFP-cortexillin I* cells with an anti-FLAG antibody. The cortexillin I precipitate pulls down endogenous myosin II, as indicated by western analysis with anti-FLAG and anti-myosin II heavy chain (MHC) antibodies. Results are representative of two biological replicates. Immunoprecipitation was performed on the cytosolic (soluble) and cytoskeletal fractions prepared in the same manner as for the LC-MS analysis in panel B.

to the cell equator, and these signals then recruit the contractile machinery to the cell equator (Kee et al., 2012). Although there is genetic and biophysical data supporting these roles, the biochemical mechanism of regulation remains unclear.

Furthermore, the molecular mechanism through which mechanoresponsive proteins accumulate at the sites of stress in the cortex is poorly understood. One possibility is that diffusion-dependent encounters with the cortex allows for proteins to bind

the cytoskeletal network individually, eventually leading to accumulation. Alternatively, pre-assembled complexes, or ‘assembly kits’, of mechanoresponsive proteins may exist in the cytoplasm, ready to engage with the cortical network upon the detection of two events: (1) when they encounter the cortex upon diffusion and (2) when they sense a specific chemical or mechanical signal. These assembly kits would then be unpacked, providing all the necessary components for a mechanoresponse, thus permitting

a faster response to mechanical stress than if the proteins had to accumulate individually. However, such a view of the mechanoreponse has not been explored.

Here, we took a proteomics approach to identify the components of the mechanobiome by detecting interactors of cortexillin I and IQGAP2. Once the components were identified, we used a combination of quantitative approaches to measure binding affinities and stoichiometries of the biochemical interactions of the contractility controller within the cytoplasm. Performing these studies within the cytoplasm provided a physiologically relevant environment and the opportunity to measure these interactions under genetic and pharmacological perturbations. We find that myosin II, IQGAP2 and cortexillin I bind to each other in the cytoplasm, and that the myosin II–cortexillin I interaction is likely responsible for their cooperative mechanoaccumulation. IQGAP1, in turn, acts as a competitive inhibitor of the cortexillin I–IQGAP2–myosin II complexes, explaining its role as a negative regulator of mechanosensing and contractility. Moreover, pre-formed cortexillin I–IQGAP2–myosin II complexes, or mechanoresponsive contractility kits (MCKs), exist in the cytoplasm, primed to detect signaling cues to respond to a stress. This MCK concept helps explain how so many proteins can accumulate rapidly and synchronously in response to discrete cues, such as from the mechanical stresses that promote mechanoaccumulation. In addition, through the proteomics approach, we identified new components of the mechanobiome, including a metabolic enzyme, RNA-binding proteins and lectins, which will further reveal the complexity of the control system.

RESULTS

Identification of direct, biochemical interactions within the mechanobiome

We first identified the molecular interactions that might be central to the mechanobiome using a proteomics approach in *Dictyostelium*. We used immunoprecipitation followed by liquid chromatography–mass spectrometry (LC–MS) to detect biochemical interactors of two key nodes, IQGAP2 and cortexillin I. We used cytoskeletal fractionation to identify protein interactions in the cytoplasm and in the cortical cytoskeleton. By doing so, we aimed to increase the likelihood of identifying key interactors, which could differ between these cellular compartments. Performing LC–MS on cytosolic and cytoskeletal precipitates of FLAG–GFP–IQGAP2 in a *iqg2*-null and FLAG–GFP–cortexillin I in a *cortI* (encoding cortexillin I)-null allowed us to identify relevant molecular complexes, as well as novel regulators of contractility. As cortexillins are major interactors of the IQGAPs (Faix et al., 2001), we also carried out proteomic analysis on IQGAP2-binding proteins in a *cortI* and *cortII* double-null (hereafter *cortII*-null) background to identify cortexillin-independent interactions. G-score analysis identified 51 and 24 unique binding partners of cortexillin I and IQGAP2, respectively (Tables S1, S2). Consistent with previous reports, we confirmed the IQGAP2–cortexillin I interaction, as well as cortexillin I interactions with Rac1A, IQGAP1 and cortexillin II, thereby validating our approach (Faix et al., 1998, 2001; Lee et al., 2010; Mondal et al., 2010). Interestingly, IQGAP1 did not co-precipitate with IQGAP2, suggesting that there are two separate cellular pools of cortexillin I–IQGAP complexes.

We compared the significant hits with other proteins we have previously implicated in the mechanobiome, generating a list of 14 potential interactors of cortexillin I and IQGAP2 (Fig. 1B). Interestingly, several hits were previously discovered through genetic suppression selections in *Dictyostelium*. We detected methylmalonate-semialdehyde dehydrogenase (mmsdh), an

enzyme that catalyzes the production of propionyl- and acetyl-coA, as an interactor of cortexillin I (Table S1). Overexpression of mmsdh was previously shown to suppress the dominant-negative phenotype of a myosin II phosphomimetic in *Dictyostelium* (Ren et al., 2014). RNA-binding protein 1B (RNP-1B) was also identified as a binding partner of cortexillin I (Table S1), which is curious since overexpression of the related protein RNP-1A suppresses the effect of nocodazole on growth of *Dictyostelium* (Zhou et al., 2010; Ngo et al., 2016). The galactose-binding lectin discoidins, which were previously demonstrated to be genetic suppressors of the phenotype of *cortI*-null cells (Robinson and Spudich, 2000), were detected as interactors with IQGAP2 by proteomics in the presence of cortexillin I and II (Table S2).

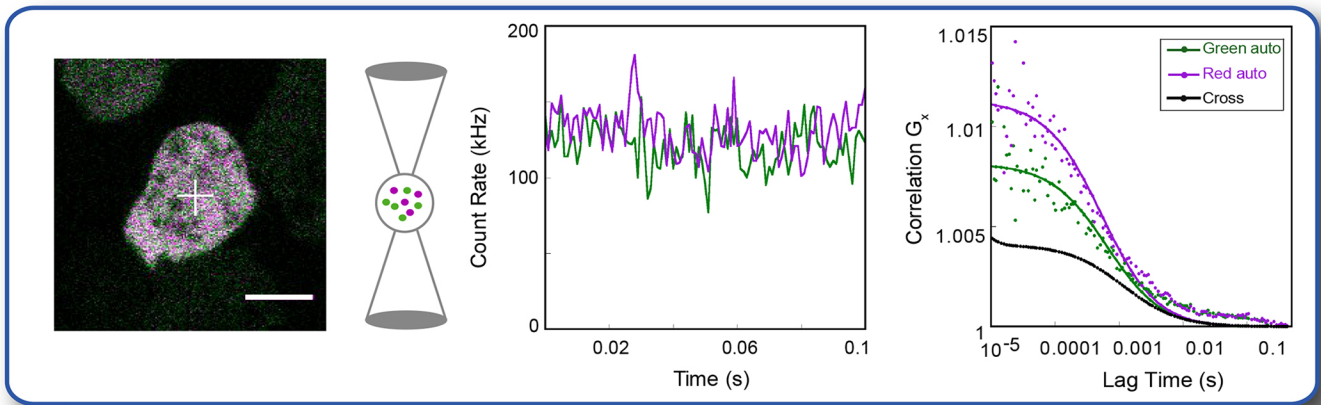
In addition, several cytoskeletal proteins emerged as cortexillin I and IQGAP2-binding partners and were detected in the absence of actin, suggesting they directly interact or exist in complexes within the cytoplasm independently of actin filaments (Tables S1–S3). Actin precipitated in the cytosolic fraction of cortexillin I, which is expected since cortexillin I is known to bind and cross link filamentous actin. However, actin was undetectable in the cytoskeletal fraction of the cortexillin I precipitate, which was isolated through salt extraction of the initial pellet isolated during preparation of the cytosolic fraction. In this cortexillin I cytoskeletal fraction, we still detected interactions with myosin II, cortexillin II, IQGAP1, IQGAP2, Rac1A and RNP-1B, indicating that these are not simply indirect interactions occurring through the actin cytoskeletal network (Table S1). In addition, actin was absent from the soluble precipitate of IQGAP2 in the complemented *iqg2*-null and *cortII*-null background, where interactions with myosin II, the capping protein acpB, and cell division cycle protein 48 were still detected (Tables S2, S3).

Importantly, myosin II (heavy chain and the essential light chain) emerged as a strong interactor of cortexillin I and IQGAP2 in the cytoskeletal and cytosolic fractions (Fig. 1B; Tables S1, S2), suggesting that large multi-protein complexes exist within the cell cortex and cytoplasm. The IQGAP2–myosin II interaction was preserved in the *cortII*-null background, indicating that this association occurs independently of cortexillin (Table S3). The saturating Mg^{2+} •ATP conditions during the immunoprecipitations, which minimize stable myosin II–actin binding, and the absence of actin in the cortexillin I cytoskeletal fraction and IQGAP2 cytosolic fraction precipitates, indicate that actin is not necessary for these interactions. We also validated the cortexillin I–myosin II association through co-immunoprecipitation with FLAG–GFP–cortexillin I in the cytosolic and cytoskeletal fractions (Fig. 1C). Given the importance of cortexillin I, IQGAP2 and myosin II in the contractility controller, we next characterized these interactions *in vivo*, studying their associations in the relevant context, rather than in cell lysates.

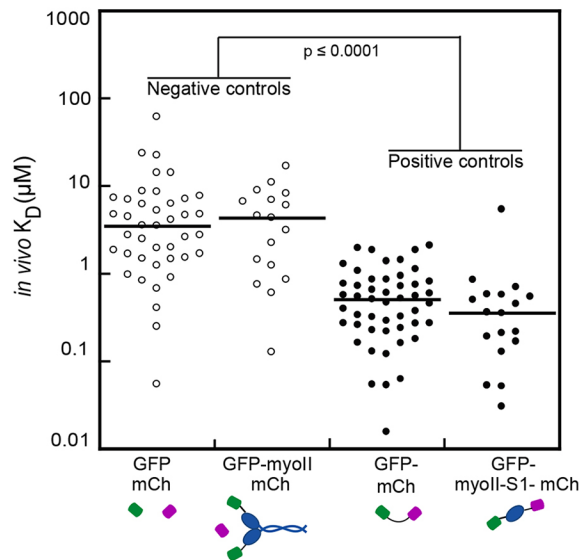
Cortexillin I and IQGAP2 interact with myosin II *in vivo*

We used fluorescence cross-correlation spectroscopy (FCCS) in live interphase cells to quantitatively characterize key protein interactions identified through mass spectrometry within their native cytoplasmic environment. With FCCS, we monitored the correlation between intensity fluctuations of two fluorescently labeled proteins expressed in cells over time. A positive cross-correlation between the fluorophores suggested an association between the two species, from which quantitative parameters such as binding affinities, concentrations and diffusion times were extracted (Bacia et al., 2006; Bacia and Schwille, 2007; Bierbaum and Bastiaens, 2013; West-Foyle et al., 2018) (Fig. 2A). Interactions were measured in each corresponding complemented-null background wherever possible to account for unlabeled protein in

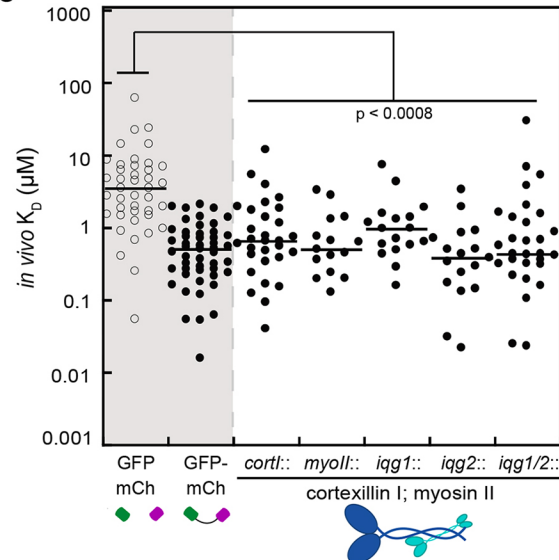
A



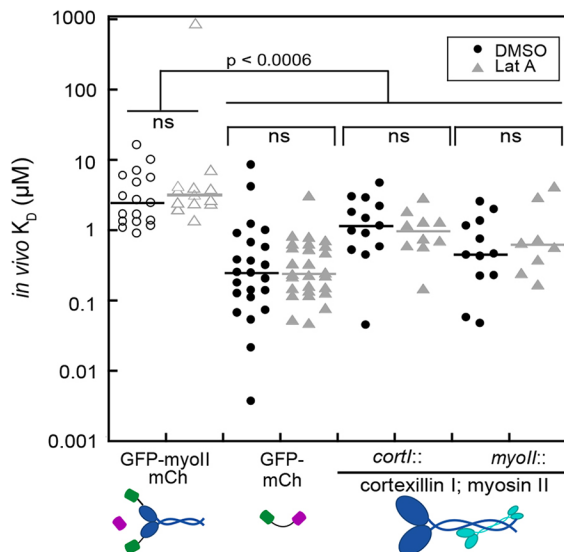
B



C



D



E

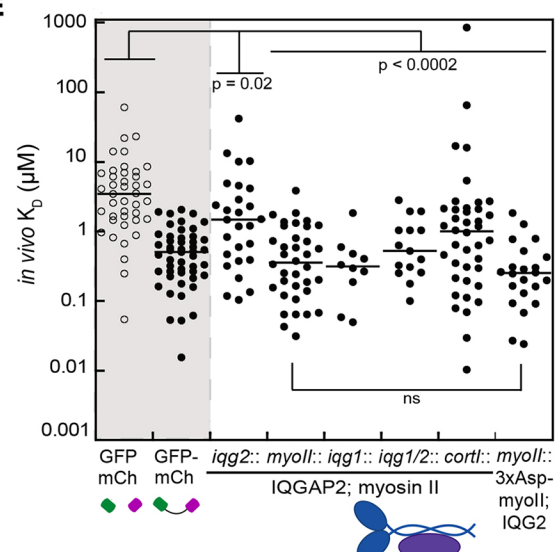


Fig. 2. See next page for legend.

the cell. Since the apparent (i.e. *in vivo*) K_D values are measured in a highly crowded and mechanically heterogeneous cytoplasm where proteins can form multiple complexes, they are not necessarily

comparable to K_D values that would be measured *in vitro* with purified components. However, we have found that for at least some proteins (14-3-3 and myosin II), the *in vivo* K_D measured by FCCS

Fig. 2. Cortexillin I and IQGAP2 interact with myosin II in the cytoplasm as detected by FCCS. (A) Schematic depicting FCCS. A representative fluorescence image of a *cortI*-null *Dictyostelium* cell expressing a linked GFP–mCherry construct. The plus sign indicates the region of confocal volume imaged. Confocal volume, indicated in gray, represents acquisition of fluorescent particles in the confocal volume. Corresponding fluorescence fluctuations recorded, and auto-correlation and cross-correlation traces are depicted. (B) Apparent, or *in vivo*, K_D for negative and positive controls indicated. A fusion GFP–mCherry or GFP–myosin II S1–mCherry both show positive cross-correlations and apparent K_D values in the submicromolar range. (C) FCCS detects interactions between cortexillin I and myosin II in various genetic backgrounds. (D) Treatment with 5 μ M Latrunculin A does not alter the *in vivo* K_D values between cortexillin I and myosin II. (E) IQGAP2 and myosin II also interact by FCCS. While the interaction is lost in an *iqg2*-null, it is restored upon removal of IQGAP1 (*iqg1*- and *iqg1/2*-null). Similar *in vivo* K_D values are measured in a *myoII*-null with either wild-type or an assembly-deficient myosin II (myosin II 3xAsp), indicating that the interaction is independent of wild-type myosin II assembly. Negative and positive controls (shaded) are reproduced from B for side by side comparison. Lines represent median values. *P*-values are derived from Kruskal–Wallis followed by a Wilcoxon–Mann–Whitney test, comparing to the GFP and mCherry negative control. ns, not significant. Data from controls is also shown in Fig. 3. Open circles indicate non-interactors.

and the *in vitro* K_D measured by biochemical assays closely agree (West-Foyle et al., 2018).

We first measured *in vivo* K_D values of positive and negative controls to assess the dynamic range of FCCS in our system. As a negative control and lower limit for binding, cells co-expressing GFP or GFP–myosin II with mCherry gave *in vivo* K_D values of 3.5 μ M (Fig. 2B). In contrast, cells where GFP was directly linked to mCherry by either a 5-amino-acid flexible linker or through the myosin II-S1 fragment showed *in vivo* K_D values of 0.50 μ M (Fig. 2B), representing positive controls, or maximum binding. We found that protein concentration did not correlate with the *in vivo* K_D within our measurable range (Fig. S1). Next, we measured the *in vivo* K_D between cortexillin I and myosin II to be \sim 0.6 μ M in *myoII*-null and *cortI*-null backgrounds, indicating their presence within the same complexes *in vivo*. Importantly, this interaction was maintained in *iqg1*-, *iqg2*- and *iqg1/2*-null backgrounds (*in vivo* K_D values of 0.96, 0.38 and 0.42 μ M, respectively) (Fig. 2C). Thus, the cooperative mechanoresponsiveness of myosin II and cortexillin I that is retained in an *iqg1/2*-null background (Kee et al., 2012; Luo et al., 2012) is likely due to their association in these complexes, or mechanoresponsive contractility kits (MCKs).

We also examined the correlation times for myosin II and cortexillin I in *cortI*- and *myoII*-null backgrounds to identify any changes in protein mobility with endogenous protein levels. While myosin II mobility was unchanged, cortexillin I has higher mobility (lower correlation time) in the *myoII*-null background where there is unlabeled cortexillin I (Fig. S2A). The unlabeled cortexillin I in the *myoII*-null likely competes for myosin II binding, which would result in a more mobile labeled cortexillin I pool, thus suggesting that myosin II might be a limiting factor in the complex. Consistent with this, from the fluorescent particle counts, the concentrations of cortexillin are generally equal to or in slight excess of myosin II (note, all *in vivo* protein concentrations and *in vivo* K_D values are summarized together in Table S4). Stoichiometric ratio differences may be further intensified as myosin II is thought to assemble into bipolar filaments through addition of dimers of myosin II functional monomers where a functional monomer is the hexamer of two heavy chains and four light chains (Luo et al., 2012; Luo and Robinson, 2015).

Since immobile proteins do not diffuse sufficiently to generate a meaningful auto-correlation signal, FCCS is unlikely to probe proteins bound to the actin network. Consistent with this,

depolymerizing actin with Latrunculin A did not alter the cortexillin I–myosin II *in vivo* K_D , indicating that interactions detected by FCCS are independent of the actin network (Fig. 2D). However, Latrunculin A treatment did decrease the mobility of myosin II in the *cortI*-null background (Fig. S2B). If indeed more myosin II–cortexillin I complexes are formed in the *cortI*-null, changing the cytoskeletal architecture of the cells may release bound complexes from the network, causing a detectable mobility shift in myosin II.

We then turned to the cortexillin-binding partner IQGAP2, which relieves IQGAP1-mediated inhibition of myosin II mechanoresponsiveness (Kee et al., 2012). We detected a positive interaction between IQGAP2 and myosin II by FCCS when complementing a *myoII*-null (*in vivo* K_D of 0.36 μ M), but the interaction was much weaker in an *iqg2*-null (*in vivo* K_D of 1.5 μ M) (Fig. 2E). Removing IQGAP1 from the cell restored the interaction (0.31 and 0.53 μ M in *iqg1*- and *iqg1/2*-nulls), implicating IQGAP1 as an inhibitor of the IQGAP2–myosin II complex and providing a biochemical basis for antagonism by IQGAP1 in the myosin II mechanosensory system (Kee et al., 2012). IQGAP2 and myosin II also associate in a *cortI*-null (*in vivo* K_D of 0.85 μ M), reproducing results seen in a *cortI/II*-null by mass spectrometry (Fig. 2E; Table S3). IQGAP2 also interacts with an assembly-deficient phosphomimetic myosin II, myosin-3xAsp, indicating that the IQGAP2–myosin II binding is independent of wild-type myosin assembly (Egelhoff et al., 1993) (Fig. 2E). The correlation times of myosin II increase upon overexpression of IQGAP2 in a *myoII*-null, suggesting increased complex formation (Fig. S2C). For IQGAP1 to prevent or disassemble the IQGAP2–myosin II complexes through competition, IQGAP1 could also interact with myosin II, which we detected by FCCS (*in vivo* K_D of 0.28 μ M) (Fig. S2D).

Regulatory proteins also interact with the contractility controller

In addition to characterizing the core components of the contractility controller, we also measured the binding affinities of several other interactions identified through the proteomics effort. Filamin interacted with cortexillin I and IQGAP2 as determined by FCCS (*in vivo* K_D values of 0.40 and 0.69 μ M, respectively) (Fig. S3A). Although Rac1A was found to be an interactor of cortexillin I through proteomics, this interaction could not be detected by FCCS (*in vivo* K_D of 1.8 μ M, not statistically significantly different from the negative control due to the width of the distribution), which could be due to the presence of both active and inactive populations of Rac1A and speaks to the sensitivity of mass spectrometry. However, IQGAP2 did weakly interact with Rac1A in a complemented *iqg2*-null and a *cortI*-null (*in vivo* K_D values 1.5 and 1.3 μ M, respectively), but failed to interact in the absence of IQGAP1 (*in vivo* K_D of 12 μ M) (Fig. S3B). Either IQGAP1 is required for the Rac1A–IQGAP2 interaction, or increased competition from myosin II or cortexillin I in the *iqg1*-null prevents detection of the interaction. By means of FCCS, we also detected mmsdh interactions with cortexillin I, as suggested by mass spectrometry, and with myosin II (*in vivo* K_D values of 1.5 and 0.87 μ M, respectively) (Fig. S3C). RNP-1A also interacts with cortexillin (*in vivo* K_D of 0.33 μ M), and the discoidin complex subunit 1A associates with cortexillin I and IQGAP2 (*in vivo* K_D values of 1.6 and 1.5 μ M, respectively) (Fig. S3C,D). The *in vivo* biochemical confirmation of these interactions emphasizes that the combined proteomics and FCCS approach is appropriate not only for identifying the cytoskeletal proteins, but also the regulatory proteins that are likely critical for the function of the contractility controller. We next focus on deciphering the mechanism of one of the key negative regulators of the contractility controller, namely IQGAP1.

IQGAP1 inhibits the interaction between cortexillin I and IQGAP2

We used FCCS to determine whether IQGAP1 has a similar inhibitory effect on the IQGAP2–cortexillin I interaction. We found an association between IQGAP2 and cortexillin I in a complemented *cortI*-null (*in vivo* K_D of 0.38 μ M), and in the absence of myosin II (*in vivo* K_D of 0.21 μ M), but not in the complemented *iqg2*-null (*in vivo* K_D of 2.7 μ M) (Fig. 3A). Competition from unlabeled cortexillin I in the *iqg2*-null may prevent detection of an interaction, implicating IQGAP2 as the limiting factor for this complex. Consistent with this, distribution of the correlation times for cortexillin I is weakly bimodal ($P=0.045$), suggesting a population of bound and unbound protein, while correlation times for IQGAP2 increase from the *cortI*-null to the *iqg2*-null (Fig. 3B). In addition, endogenous IQGAP1 may compete with IQGAP2 for binding cortexillin I. In line with this idea, removing IQGAP1 increased the binding affinity between IQGAP2 and cortexillin I by 30-fold, shifting the *in vivo* K_D to 0.12 μ M in an *iqg1/2*-null (Fig. 3A). Moreover, the correlation times of IQGAP2 and cortexillin I increased 7–18-fold over that seen with the *cortI*-null, reflecting much larger complexes in the cytoplasm of an *iqg1/2*-null (Fig. 3B). These drastic changes in affinities and correlation times were unperturbed upon treatment with Latrunculin A, indicating that the shifts are not due to interactions with the actin network or the formation of complexes sufficiently large to be restricted by the actin meshwork pore size (Fig. S4A,B). Since cortexillin I binds IQGAP1 as well (Faix et al., 2001) (Fig. S2D), to further probe the

formation of the MCKs in the cytoplasm, we examined the stoichiometries of the individual interactions.

Quantifying the stoichiometries of core building blocks

We used Single-Molecule Pull-down (SiMPull) to quantify the stoichiometries of cortexillin I, IQGAP2 and IQGAP1 in these cellular complexes (Jain et al., 2011; Aggarwal and Ha, 2014). Briefly, we immunoprecipitated protein complexes containing two distinct fluorescently labeled proteins on antibody-coated slides. We visualized isolated complexes at single-molecule resolution via total internal reflection fluorescence (TIRF) microscopy to quantify fluorophore colocalization (binding) and photobleaching events (oligomerization state) (Fig. 4A). We used cells expressing GFP–mCherry (linked) and merges of different regions to determine maximum and background colocalization percentage, respectively (Fig. 4B). Owing to incomplete maturation of GFP and mCherry, maximum colocalization is ~60% (Jain et al., 2011). Colocalization is quantified as the percentage of immunoprecipitated spots with which the opposite fluorophore co-precipitated (Fig. 4B; Fig. S5A). The high degree of colocalization of mCherry–cortexillin I with GFP–IQGAP1 and GFP–IQGAP2 using antibodies against GFP, RFP and cortexillin I further confirmed cortexillin I binding to IQGAP1 and IQGAP2, and motivated analysis of the stoichiometries of these complexes (Fig. 4B; Fig. S5B).

The linked and unlinked GFP and mCherry showed ~20% two-step photobleaching, while the known dimeric protein 14-3-3–GFP showed 35% two-step photobleaching in our experiments (Fig. 4). The mean plus two standard deviations of the linked and unlinked

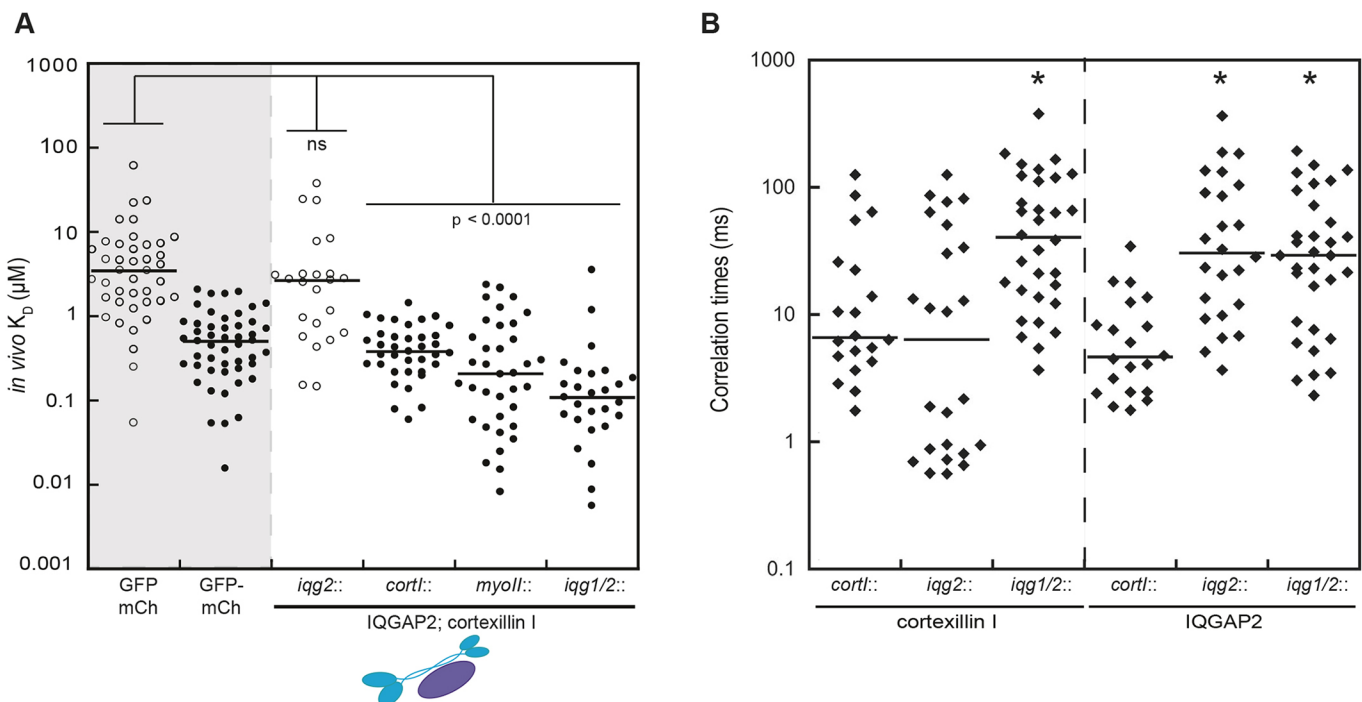


Fig. 3. IQGAP1 inhibits the IQGAP2–cortexillin I interaction. (A) FCCS measurement of *in vivo* K_D values demonstrate that IQGAP2 and cortexillin I interact in the *cortI*-null complemented background, and in the absence of myosin II. The binding is lost in the *iqg2*-null complemented cell, but the affinity between IQGAP2 and cortexillin I increases significantly in an *iqg1/2*-null. P values are derived from Kruskal–Wallis followed by a Wilcoxon–Mann–Whitney test as compared to the GFP and mCherry negative control. ns, not significant. Negative and positive controls (shaded) are reproduced from Fig. 2B for side by side comparison. (B) Correlation times in cell lines coexpressing labeled cortexillin I and IQGAP2. The correlation time increases for cortexillin I from the *cortI*- to *iqg1/2*-null, and increases for IQGAP2 in both the *iqg2*- and *iqg1/2*-null backgrounds, suggesting formation of larger complexes. The correlation time for cortexillin shifts to a bimodal distribution in the *iqg2*-null ($P=0.045$ by Hartigan's dip test on log-transformed data), indicating a population of bound and unbound cortexillin I caused by endogenous cortexillin I. * $P<0.001$. P values are derived from Kruskal–Wallis followed by a Wilcoxon–Mann–Whitney test as compared to the correlation time in the *cortI*-null background. Open circles indicate non-interactors. Lines represent the median values.

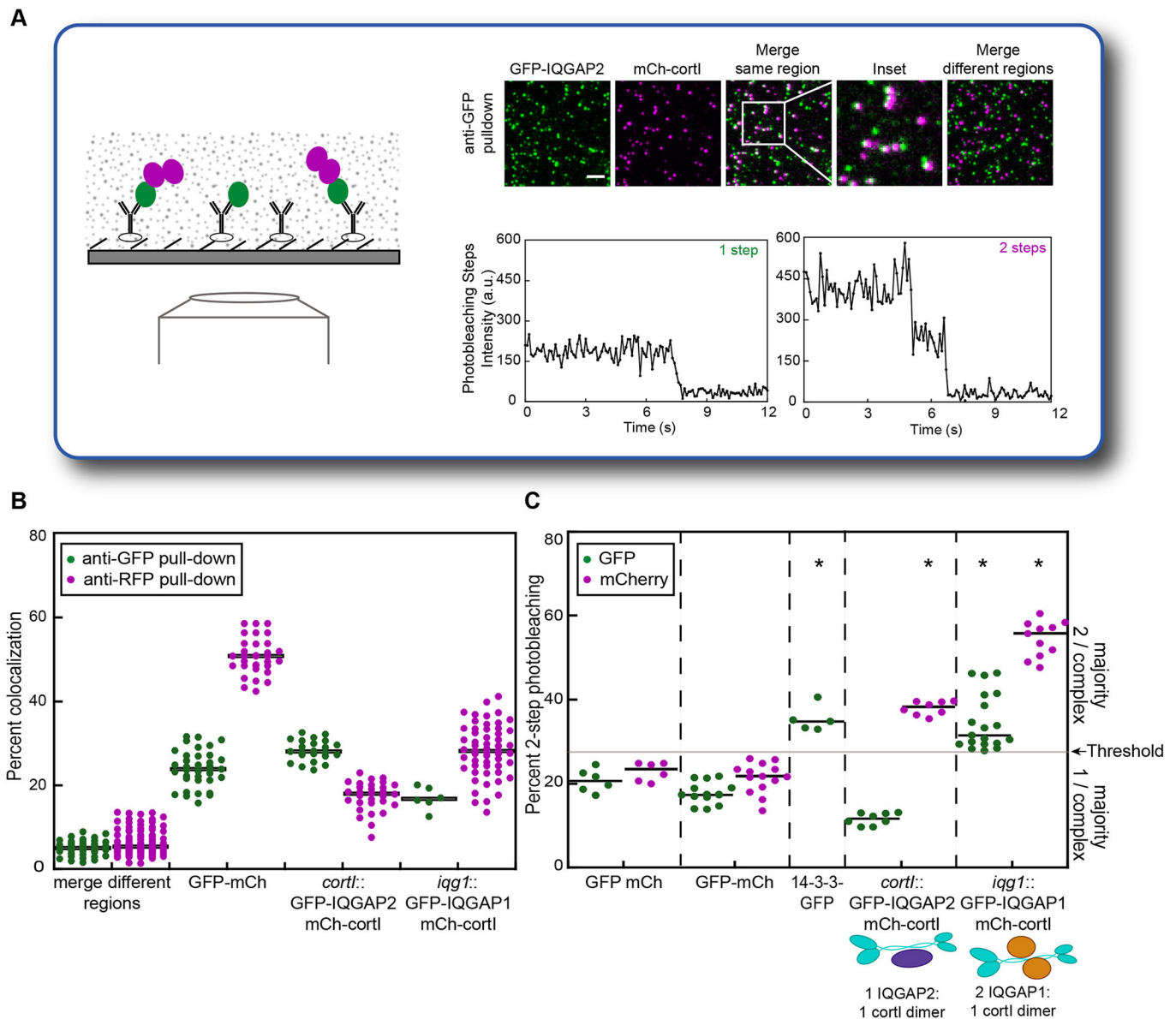


Fig. 4. IQGAP1 and IQGAP2 bind cortactin I with different stoichiometries. (A) Schematic of SiMPull. Lysate is flowed over a PEG-passivated slide coated with biotinylated antibody bound through NeutrAvidin. Antibody binds one protein that co-precipitates the interacting protein resulting in colocalization of single fluorescent spots imaged by total internal reflection fluorescence (TIRF) microscopy. Merge images of different non-overlapping regions controls for random colocalization. The number of photobleaching steps per fluorescent spot reveals the stoichiometry in the complex. Scale bar: 5 μ m. (B) Quantification of complex formation using colocalization. The percentage colocalization of cortactin I with IQGAPs 1 and 2 indicate complex formation as determined by anti-GFP (green) and anti-RFP (magenta) antibody pull-downs. Colocalization from linked GFP and mCherry and merge of different regions are shown for comparison. (C) GFP, mCherry and the fused GFP-mCherry show ~20% two-step photobleaching, indicative of a complex with primarily one subunit. 14-3-3-GFP, a stable dimer, has two-fold higher level of two-step photobleaching, reflecting the dynamic range of the technique. Fluorophore maturation accounts for the ~60% maximum, typical of this technique (Husbands et al., 2016). * $P \leq 0.005$ by ANOVA followed by a Fisher's LSD, as compared to the GFP and mCherry monomers. Lines represent median values. The gray line represents the mean+2 s.d. of the GFP and mCherry fluorophores, reflecting a threshold above which medians represent a majority of two molecules per complex. Each data point represents a measurement from a single image, with ~200–800 molecules per image. At least three images were collected per sample per biological replicate. Number of biological replicates: 14-3-3=1; GFP and mCherry unlinked=2; GFP-mCherry=3; cortactin I-IQGAP2=3; cortactin I-IQGAP1=3.

fluorophores was 27%, and thus, we considered 27% two-step photobleaching as a threshold whereby proteins that scored above or below this level were considered predominantly dimeric or monomeric, respectively. Based on these metrics, we conclude that both cortactin I and IQGAP1 form complexes with two subunits each, while just a single IQGAP2 molecule forms a complex with a cortactin I dimer (Fig. 4C). No events with greater than two-step photobleaching were recorded, thereby ruling out any

higher-order assemblies. Overall, IQGAP1 may negatively regulate mechanoresponsiveness by sequestering away binding sites on cortactin I, preventing the formation of the cortactin I-IQGAP2-myosin II mechanoresponsive contractility kits.

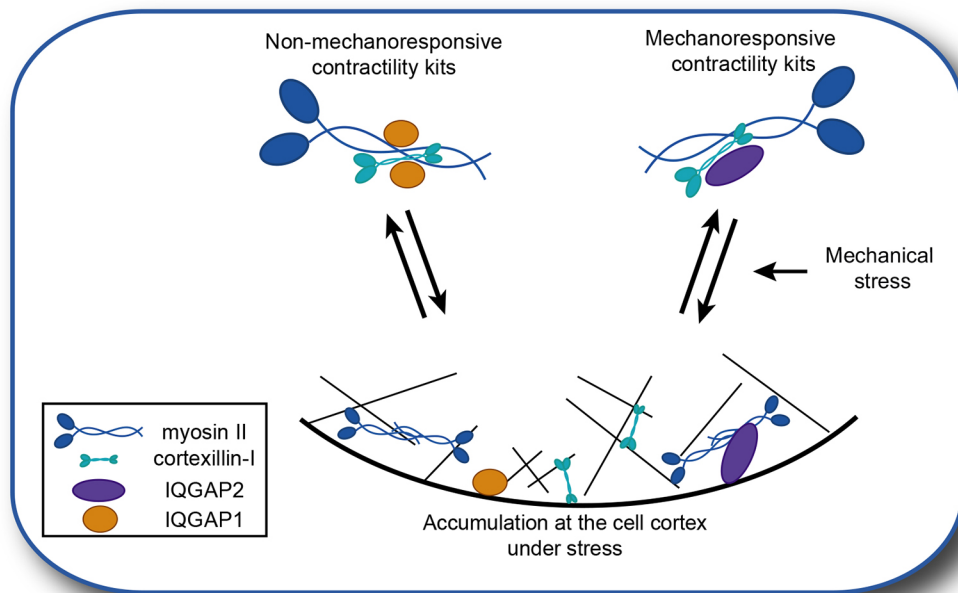
DISCUSSION

In this study, we built from an unbiased mass spectrometry analysis to highlight previously unappreciated components of the

mechanobiome and to characterize the biochemical interactions that drive the contractility controller (Fig. 5). The combination of proteomics and quantitative *in vivo* biochemical analysis indicates

that myosin II and cortexillin I form complexes in the cytoplasm, providing a biochemical basis for their cooperative mechanoaccumulation (Luo et al., 2012). The IQGAPs also bind

A



B

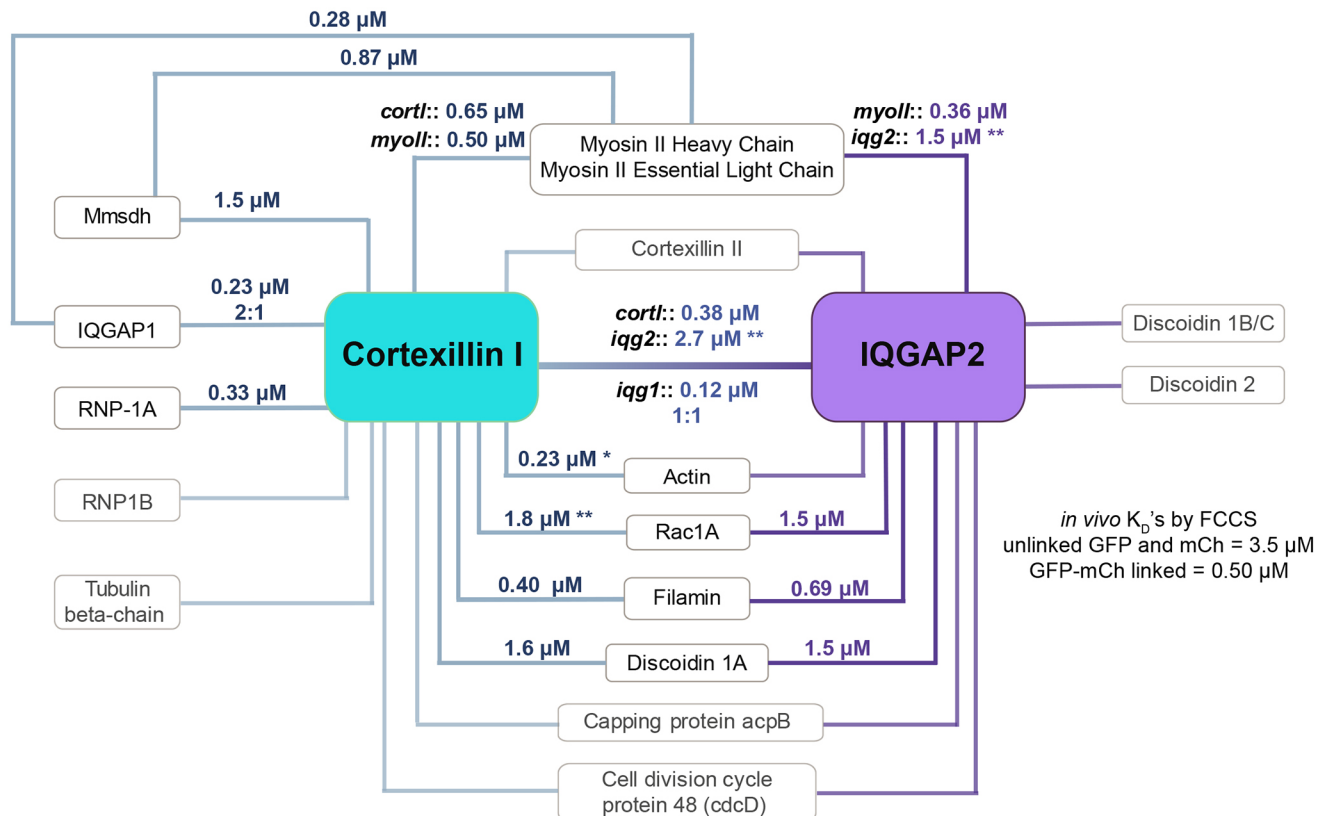


Fig. 5. The network of biochemical interactions in the contractility controller. (A) Schematic depicting non-mechanoresponsive and mechanoresponsive contractility kits (MCKs). Mechanical stress induces increased accumulation of MCKs to the cortex. (B) Mechanobiome map representing protein interactions detected by proteomics and confirmed either by biochemical, genetics or biophysical assays. Apparent *in vivo* K_D values measured by FCCS, and stoichiometries measured by SiMPull. Interactions between RNP1A and cortexillin I and between filamin and IQGAP2 were not detected by mass spectrometry but were demonstrated by FCCS. * Indicates previously measured *in vitro* K_D (Faix et al., 1996). ** Interactions not significantly different from negative control as determined by FCCS.

the cortexillin I–myosin II complexes, providing key regulation of these mechanoresponsive proteins. Although myosin II has not been shown to interact biochemically with cortexillin I or IQGAP2 in *Dictyostelium* previously, myosin has been shown to bind the IQGAP2 paralog, Rng2, in *Schizosaccharomyces pombe* (Laporte et al., 2011; Laplante et al., 2016). Moreover, mammalian IQGAP1 interacts with non-muscle myosin II essential light chain through its IQ motif *in vitro* (Weissbach et al., 1998) (although it should be noted that the *Dictyostelium* IQGAPs do not contain the IQ motif). Thus, the ability of IQGAPs to interact with myosin II proteins appears to be a highly conserved function, spanning a billion years of evolution. Perhaps it is of no surprise then that IQGAPs provide such an essential role in the contractility controller.

The cortexillin I–IQGAP2–myosin II complexes appear to be the functional unit of these proteins that then engages with the cytoskeletal network. In fact, the concept that proteins pre-form into complexes in the cytoplasm has precedence. Myosin II, for example, exists in the cytoplasm as a functional hexamer, with two essential and two regulatory light chains bound to a dimeric heavy chain. It would be impractical for the cell to mount a response to a mechanical stress input, which propagates on the timescale of sub- to low numbers of seconds, if it had to assemble each heavy chain and light chain independently. Scaling up, the cell appears to use this same strategy of utilizing pre-assembled complexes by creating kits of cortexillin I–IQGAP2–myosin II (MCKs) (Fig. 5), which are then primed to be rapidly activated when the appropriate chemical or mechanical stimulus is experienced.

To ensure that the system it is not overly mechanosensitive, IQGAP1 serves as a competitive inhibitor of IQGAP2 for cortexillin I and myosin II. While IQGAP1 is thought to bind the C-terminal domain of cortexillin I and IQGAP2 binds the N-terminal domain of cortexillin I, it is possible that interactions with two IQGAP1 molecules occlude the binding sites on cortexillin I for IQGAP2 (Faix et al., 2001; Mondal et al., 2010). IQGAP1 also impedes the formation or promotes the disassembly of the MCKs to create a population of free, unbound IQGAP2 monomers, thereby attenuating the sensitivity of the controller. Moreover, interactions between cortexillin I, IQGAP2, activated Rac1A and filamin provide further spatial and temporal regulation of the controller (Faix et al., 2001; Mondal et al., 2010).

Detecting interactions between the contractility controller and several unexplored proteins by proteomics and FCCS suggests that the mechanobiome consists of a network of proteins that integrates feedback from various seemingly unrelated processes. For example, mmsdh, an enzyme in the valine degradation pathway, may facilitate feedback between metabolism, nutrient sensing and cell mechanics, and such cross talk between these fundamental cellular mechanisms has been uncovered in other systems (Bays et al., 2017; Hamann et al., 2017). Since the RNP proteins were initially discovered as a genetic suppressor of nocodazole, these RNPs may provide crosstalk between microtubules and the actin cytoskeletal network (Zhou et al., 2010; Ngo et al., 2016). The discoidins, which are traditionally considered lectins, may link the plasma membrane to the cytoskeletal network. The presence of these proteins in the mechanobiome reveals that the contractility controller does not function in isolation, but rather in concert with various cellular processes. Our work has demonstrated that multiple regulatory features of the mechanobiome are crucial for allowing the cell to robustly adapt to its changing environment.

In the textbook model, cytokinesis is a process driven by the contractile actomyosin ring that forms at the cleavage furrow. However, a number of studies have revealed that a complex

meshwork of actin filaments, myosin II bipolar filaments, actin crosslinkers and regulatory proteins promotes accurate cleavage furrow ingression, actively tuning the protein amounts and mechanical properties (power output, viscoelasticity and strain stiffening) of the contractile machinery in *Dictyostelium* (Effler et al., 2006; Reichl et al., 2008; Kee et al., 2012; Luo et al., 2012; Srivastava and Robinson, 2015), *Caenorhabditis elegans* (Descovich et al., 2018) and mammalian systems (Manukyan et al., 2015; Schiffrhauer et al., 2016). Our work reveals key biochemical interactions that are critical for the contractility controller and emphasizes that the mechanobiome is composed of more than just actin-binding cytoskeletal proteins.

While the integration of chemical and mechanical signaling may vary in different processes, the mechanobiome is not only applicable to cytokinesis. Deciphering the regulation and activity of the contractility machinery has been critical for understanding many diverse processes, including cell migration (Lee et al., 2010), epithelial tube morphogenesis in *Dictyostelium* (Dickinson et al., 2012), hepatocyte mechanics (Bai et al., 2016), entosis (Sun et al., 2014; Hamann et al., 2017), myoblast fusion (Kim et al., 2015; Duan et al., 2018) and cancer metastasis (Surcel et al., 2015, 2017 preprint). Elucidation of the molecular mechanisms that govern the positive and negative regulation of cell shape change will reveal a greater insight into normal development and the underlying biology of human disease states.

MATERIALS AND METHODS

Reagents

The plasmids for GFP–mCherry (linked), and GFP- and/or mCherry-tagged fusions of myosin II, myosin II 3xAsp, cortexillin-I, IQGAP1, IQGAP2, mmsdh, Rac-1A, filamin and RNP-1A have been described previously (Effler et al., 2006; Lee et al., 2010; Zhou et al., 2010; Kee et al., 2012; Luo et al., 2013; West-Foyle et al., 2018). For the FLAG constructs, FLAG–GFP was cloned into the pDRH plasmid using the *Bgl*II and *Sal*I restriction sites, and cortexillin I or IQGAP2 were added between the *Sal*I and *Not*I restriction sites. GFP–myosin-II-S1–mCherry pDM181 was built by cloning the myosin II S1 fragment into GFP–pDM181 between the *Sal*I and *Not*I sites, and subsequently inserting mCherry between *Not*I and *Mlu*I sites. Discoidin-1A was cloned by PCR using template genomic DNA from the WT strain KAx3 with forward primer 5'-GTGCACATGTCTACCCAA-GGTTTAGTTCAACTCTCG-3' (including a 5' *Sal*I site), and reverse primer 5'-GCGGCCGCTTATTCCAAAGCGGTAGCAATGTAATCAG-3' (including a 3' *Not*I site). The *Sal*I and *Not*I sites were then used to clone the gene into GFP–pDM181. The monoclonal antibody 241-438-1 against cortexillin I developed by Günther Gerisch (Max Planck Institute) was obtained from the Developmental Studies Hybridoma Bank (University of Iowa, Iowa City, IA) and used at 1:300 for SiMPull. An M2 anti-FLAG antibody and anti-FLAG affinity agarose gel (F3165 and A2220, Sigma-Aldrich, St Louis, MO) were used for immunoprecipitation. The myosin II heavy chain antibody (anti-my6) (Peltz et al., 1985) and anti-FLAG antibody were used for western blot analysis (1:10,000 and 1:1000, respectively). Biotinylated rabbit anti-GFP (600-406-215, Rockland Immunochemicals, Pottstown, PA), rabbit anti-RFP (ab34771, Abcam, Cambridge, UK), and rabbit anti-HA (ab26228, Abcam) antibodies were used at 1:300 for SiMPull. Latrunculin A was obtained from Sigma-Aldrich.

Cell strains and culture

A complete list of the strains used is provided in Table S5. Cells were grown in Hans' enriched 1.5× HL-5 medium, enriched with 8% final minimal (FM) medium, containing penicillin and streptomycin, at 22°C on polystyrene Petri dishes. Wild-type strains used were KAx3 and rescued mutant strains. Mutant cell lines used have been previously described: *myoII*, *cortI*, *cortII*, *iqg1*, *iqg2* and *iqg1/2* (Ruppel et al., 1994; Robinson and Spudich, 2000; Lee et al., 2010). Cells were transformed with the expression plasmids by electroporation using a Genepulser-II electroporator (Bio-Rad, Hercules,

CA). Cells were then grown in selection media containing 15 µg/ml G418, 40 µg/ml hygromycin, or both drugs when transforming two plasmids. Expression levels were checked by fluorescence imaging or western blot analysis. For Latrunculin A treatment, cells were pre-treated with 0.1% DMSO for 4 h. Cells plated in imaging chambers were washed with low-flow medium (0.385% glucose, 0.178% protease peptone, 0.045% bacto-yeast extract, 3.3 mM Na₂HPO₄, 3.6 mM KH₂PO₄, pH 6.5) with 0.1% DMSO, and were incubated with 5 µM Latrunculin A diluted in low flow media for 10 min. Slides were changed after 15 min of imaging.

Anti-FLAG co-immunoprecipitation

Logarithmically growing cells (*cortI::FLAG-GFP-cortI*, *cortI::FLAG-GFP*, *iqg2::FLAG-GFP-IQGAP2*, *iqg2::FLAG-GFP*; *cortI/II::FLAG-GFP-IQGAP2*; *cortI/II::FLAG-GFP*) were collected, washed in 1× phosphate-buffered saline, and resuspended in lysis buffer (100 mM PIPES pH 6.8, 2.5 mM EGTA, 1 mM MgCl₂, 1 mM ATP, 0.1% Triton X-100, and protease inhibitor cocktail) at a cell density of 1×10⁷ cells/ml. Cells were incubated with rotation at 4°C for 30 min and lysates were centrifuged at 15,000 *g* for 5 min at 4°C to separate the soluble and cytoskeletal fractions. The pellet from the ‘cytoskeletal’ sample was dissolved in release buffer (100 mM PIPES pH 6.8, 2.5 mM EGTA, 1 mM MgCl₂, 1 mM ATP, 200 mM NaCl and protease inhibitor cocktail), and incubated on a rotator for 15 min at 4°C. The ‘cytoskeletal’ sample was then centrifuged at 15,000 *g* for 5 min at 4°C, and the supernatant was processed for co-immunoprecipitation. Lysates were pre-cleared with agarose-bead-conjugated mouse IgG (Sigma-Aldrich) for 30 min and centrifuged at 5000 *g* for 1 min. Supernatants were transferred to tubes containing 40 µl pre-washed agarose-bead-conjugated anti-FLAG antibody (Sigma-Aldrich) overnight at 4°C. The resin was washed four times with 1× TBS, and eluted with 0.1 M glycine pH 3.5 for mass spectrometry analysis or with sample buffer for western analysis.

Mass spectrometric analysis

A 40 µl volume of eluted immuno-enriched samples was incubated with 10 mM of Tris-2 carboxyethyl phosphine (Sigma) for 20 min at room temperature with shaking, followed by alkylation with 10 mM 2-iodoacetamide (IAA; Sigma) for 20 min, at ambient room temperature, protected from light. The reduced and alkylated proteins were acetone precipitated to remove solutes not compatible with downstream LC-MS analysis. The final pellet was air-dried. 5 µg of endoproteinase Lys-C (Promega, Madison, WI) was reconstituted in 650 µl of digestion solution [0.1% RapiGest (Waters, Milford, MA), 20% acetonitrile (ACN), 50 mM ammonium bicarbonate]. 20 µl of that solution was added to each acetone precipitated sample. The protein pellet was digested for 2 h at 37°C with constant shaking. Following addition of 1 µg of trypsin (Promega, Madison, WI) (1:50 trypsin:protein ratio) in 20 µl of digestion solution, enzymatic proteolysis continued overnight under the same conditions. Trifluoroacetic acid was added to deactivate enzymes. Samples were desalted using UltraMicro Spin C18 columns (NestGroup, Southborough, MA) according to the manufacturer's instructions. Collected peptides were lyophilized and reconstituted in 10 µl of water with 0.1% fluoroacetic acid (FA) Optima (Thermo Fisher Scientific, Waltham, MA).

Aliquots (4 µl each) of each tryptic protein digest solution were analyzed on a EASY n-LC 1000 (Thermo Fisher Scientific) machine coupled to an Orbitrap-Elite (Thermo Fisher Scientific) mass spectrometer. Peptides were separated on an Acclaim PepMap RSLC column (Thermo Fisher Scientific), with a 50 µm inner diameter, 15 cm length, packed with C18 reversed phase 2 µm particles, 100 Å pore size), using mobile phase linear gradient from 5% B to 20% B in 40 min continued to 35% B in 10 min at 300 µl/min flow rate, where mobile phase A was composed of 0.1% (v/v) formic acid in water and mobile phase B was 0.1% (v/v) formic acid in acetonitrile.

Eluting peptides were ionized via a Nanospray Flex ion source (Thermo Fisher Scientific) operated at the following settings: source voltage 2.00 V, capillary temperature 275.00°C and S-lens RF level 60. The Orbitrap-Elite mass spectrometer was operated in data dependent mode. MS precursor scan spectra (*m/z* 350–1800) were acquired in the Orbitrap with mass resolution of 60,000 full-width half-maximum (at *m/z* 400). The 15 most intense ions from each MS scan were automatically targeted for collision induced

dissociation (CID) fragmentation (MS/MS) in the LTQ (linear ion trap) with dynamic exclusion 90 s. For MS1, the automatic gain control (AGC) target was set to 10⁶ with a maximum accumulation time of 250 ms. Only ions of 1000 minimum signal intensity were selected for MS2 fragmentation. MS2 spectra were acquired in a rapid scan mode in the LTQ (linear ion trap) using a targeted setting of 10×10⁴ ions and accumulation time of 150 ms. Normalized collision energy was set at 35%. The default charge state was set at two. The isolation window for the ion gate was fixed at two Daltons. The activation Q was set at 0.25.

Raw MS data were searched against the UniProt *Dictyostelium discoideum* database (37,261 entries; October 2013 version) using Sorcerer 2™-SEQUEST® (Sage-N Research, Milpitas, CA) with post search analysis performed using the Trans-Proteome Pipeline, implementing PeptideProphet and ProteinProphet algorithms. Sequest (Thermo Fisher Scientific, San Jose, CA; version 1.0) was set up with the following search parameters: semi-enzyme digest using trypsin (after Lys or Arg) with up to two missed cleavages; monoisotopic precursor mass range of 400–4500 amu; and oxidation (Met), carbamidomethylation (Cys), and acetylation (Lys) were specified as variable modifications. Peptide mass tolerance was set to 50 ppm, fragment mass tolerance was set to 1 amu, fragment mass type was set to monoisotopic, and the maximum number of modifications was set to four per peptide.

Scaffold (version Scaffold_4.4.1.1, Proteome Software Inc., Portland, OR) was used to validate peptide and protein identifications. Error rates (false discovery rates) and peptide probabilities (*p*) were calculated by Peptide Prophet; accepted peptide identifications had greater than 95% probability with Scaffold delta-mass correction. Protein Probabilities were assigned by the Protein Prophet algorithm, only proteins whose identification was at a greater than 95% probability and contained at least two identified peptides were reported.

The normalized spectral counts (listed in Tables S1–S3) were used to identify proteins that were up- or down-regulated in the experimental samples as compared to the control group based on quantifying the protein total spectral count. We applied the G-test of independence to determine the significance of difference in the normalized spectral count (average of three replicates) for the experimental and control group. We defined f_1 =normalized spectral counts/protein in the control sample (FLAG-GFP), f_2 =normalized spectral counts/protein in the experimental sample (FLAG-GFP-cortexillin I, for example). When a protein was absent from one of the samples, it was assigned the normalized spectral count of 0.0001. The G value was calculated with Eqn 1:

$$G = 2f_1 \ln \left(\frac{f_1}{avgf_1} \right) + 2f_2 \ln \left(\frac{f_2}{avgf_2} \right), \quad (1)$$

where $avgf_1=avgf_2=(f_1+f_2)/2$.

A χ -squared distribution with one degree of freedom was assumed, with $P<0.05$ considered significant. Thus, a protein was considered differentially expressed if the calculated G value was greater than 3.841.

Fluorescence correlation and cross-correlation spectroscopy

Fluorescence correlation (FCS) experiments were performed on interphase cells at ambient temperature (~20–23°C, normal growth temperatures for *Dictyostelium* cells) using a Zeiss AxioObserver with 780-Quasar confocal module and FCS, with a C-Apochromat 40× (NA 1.2) water objective (Srivastava and Robinson, 2015; West-Foyle et al., 2018). 100 nM Rhodamine 6G was used for pinhole alignment and structural parameter calculation as previously described (Srivastava and Robinson, 2015). A structural parameter of 6 was used and the confocal volume was measured to be 0.45 fL. Data were fitted to a single-component 3D diffusion model, including a triplet-state component with an upper limit of 8 µs (as described in Kothari et al., 2017). For negative controls, we measured the interaction between co-expressed soluble GFP and mCherry, as well as co-expressed soluble mCherry and GFP-myosin, to compensate for the slower diffusion time of larger proteins. As positive controls, we compared the interaction between GFP attached to mCherry by a 5-amino-acid flexible linker as well as fluorophores linked by the myosin II S1 fragment. Where possible, we also switched fluorophores to ensure binding affinities were not dependent upon fluorophore interactions. In addition, to confirm the full range of the

experimental setup, we measured dual-color fluorescent beads in solution, which showed maximal auto- and cross-correlations of 0.25 and a measured K_D of 1 pM.

The *in vivo* K_D was calculated using Eqn 2, where N is Avogadro's number, V is volume, G_x is the cross-correlation and G_a and G_b refer to the auto-correlation values for GFP and mCherry as extracted from the Zen imaging software (Bierbaum and Bastiaens, 2013; Kothari et al., 2017; West-Foyle et al., 2018).

$$\text{in vivo } K_D = \frac{G_x}{N \cdot V \cdot G_a \cdot G_b} \cdot \left(\frac{G_a}{G_x} - 1 \right) \cdot \left(\frac{G_b}{G_x} - 1 \right). \quad (2)$$

A few strains were measured over 2 days, and most were measured over 3–5 days. The *in vivo* K_D values are reported in Table S4. Concentrations were calculated by using the auto-correlation to measure the number of particles in the known confocal volume of 0.45 fL and correcting for maturation time based on the fluorophore. As most of the concentration ranges were normally distributed, we have reported the concentrations as mean \pm s.e.m. (Table S4).

Single-molecule pull-down

Transformed cells were washed once in 1X phosphate buffered saline, resuspended in lysis buffer (as described above) at a cell density of 5×10^7 cells/ml. Cells were rotated at 4°C for 15 min, and centrifuged at $15,000 \times g$ for 5 min to remove cell debris. Lysate was added to slides coated with biotinylated antibodies as previously described (Husbands et al., 2016). Biotinylated antibodies immobilized in flow chambers using NeutrAvidin (Thermo Fisher Scientific) were used to pull-down one protein of interest, and single-molecule TIRF imaging with a $100\times$ objective was used to image both GFP and mCherry-labeled proteins. Areas with ~ 200 – 800 molecules were imaged to avoid overlapping fluorescence signal due to spatial proximity. Colocalization was quantified using Eqn 3 for each antibody (where X is the protein pulled down).

$$\begin{aligned} &\text{colocalization with antibody against X} \\ &= \frac{\text{number of colocalized spots}}{\text{number of X spots}}. \end{aligned} \quad (3)$$

Photobleaching analysis was performed as described (Husbands et al., 2016). Anti-HA was used as a control antibody to demonstrate low level of non-specific pull-down of fluorescently labeled proteins.

Methodology and statistics

Sample size

The normalized spectral counts listed in Tables S1–S3 for mass spectrometry refer to average values from three biological replicates. Each data point for FCCS represents the average measurement of between 3–10 traces for a single cell. Each data point for SiMPull represents a single image statistic.

Pre-established data inclusion/exclusion criteria

For FCCS, a single cell trace was only excluded if photobleaching was detected or the count rate deviated over 50%, indicating the presence of an organelle or aggregate diffusing through the confocal volume. For SiMPull, images were only excluded from analysis if molecules were pre-bleached due to an acquisition issue during the experiment.

Statistical analysis

An ANOVA followed by a Fisher's least square difference post hoc test ($\alpha < 0.05$) or Kruskal–Wallis followed by a Wilcoxon–Mann–Whitney test was used. Statistical analysis was performed using KaleidaGraph (Synergy Software) or the Hartigans' dip test for unimodality (R statistical package).

Acknowledgements

We thank the members of the D.N.R. laboratory for helpful discussions. We thank Sheil Kee for generating the GFP-myosin II S1-mCherry construct. We also thank the Johns Hopkins University Microscope Facility, particularly Barbara Smith and

Hoku West-Foyle, for providing equipment and technical assistance for FCCS experiments.

Competing interests

The authors declare no competing or financial interests.

Author contributions

Conceptualization: P.K., V.S., J.E.V.E., T.H., D.N.R.; Methodology: P.K., V.S., V.A., I.T., D.N.R.; Software: P.K.; Validation: P.K., V.S.; Formal analysis: P.K., V.S., V.A., I.T.; Investigation: P.K., V.S., V.A., I.T.; Resources: P.K., V.S., V.A., I.T., T.H., J.E.V.E., D.N.R.; Data curation: P.K.; Writing - original draft: P.K., V.S., D.N.R.; Writing - review & editing: P.K., V.A., I.T., J.E.V.E., T.H., D.N.R.; Visualization: P.K., V.S., D.N.R.; Supervision: P.K., V.S., D.N.R.; Project administration: P.K., D.N.R.; Funding acquisition: P.K., T.H., J.E.V.E., D.N.R.

Funding

This work was supported by the National Institutes of Health (R01GM66817 to D.N.R., R21AG042332 to T.H., F31GM122258 to P.K., T32GM007445 to the BCMB Graduate Program, S10 OD016374 to the JHU Microscope Facility); the Defense Advanced Research Projects Agency (HR0011-16-C-0139 to D.N.R.); the Erika J. Glazer chair in Women's Heart Health (J.E.V.E.); the Barbra Streisand Women's Heart Center (J.E.V.E.); and the Advanced Clinical Biosystems Institute (J.E.V.E.). T.H. is an investigator with the Howard Hughes Medical Institute. Deposited in PMC for release after 12 months.

Supplementary information

Supplementary information available online at <http://jcs.biologists.org/lookup/doi/10.1242/jcs.226704.supplemental>

References

- Aggarwal, V. and Ha, T. (2014). Single-molecule pull-down (SiMPull) for new-age biochemistry: methodology and biochemical applications of single-molecule pull-down (SiMPull) for probing biomolecular interactions in crude cell extracts. *BioEssays* **36**, 1109–1119.
- Bacia, K. and Schwiile, P. (2007). Practical guidelines for dual-color fluorescence cross-correlation spectroscopy. *Nat. Protoc.* **2**, 2842–2856.
- Bacia, K., Kim, S. A. and Schwiile, P. (2006). Fluorescence cross-correlation spectroscopy in living cells. *Nat. Methods* **3**, 83–89.
- Bai, H., Zhu, Q., Surcel, A., Luo, T., Ren, Y., Guan, B., Liu, Y., Wu, N., Joseph, N. E., Wang, T.-L. et al. (2016). Yes-associated protein impacts adherens junction assembly through regulating actin cytoskeleton organization. *Am. J. Physiol. Gastrointest. Liver Physiol.* **311**, G396–G411.
- Bays, J. L., Campbell, H. K., Heidema, C., Sebbagh, M. and DeMali, K. A. (2017). Linking E-cadherin mechanotransduction to cell metabolism through force-mediated activation of AMPK. *Nat. Cell Biol.* **19**, 724–731.
- Bierbaum, M. and Bastiaens, P. I. H. (2013). Cell cycle-dependent binding modes of the ran exchange factor RCC1 to chromatin. *Biophys. J.* **104**, 1642–1651.
- De Lozanne, A. and Spudich, J. A. (1987). Disruption of the Dictyostelium myosin heavy chain gene by homologous recombination. *Science* **236**, 1086–1091.
- Descovich, C. P., Cortes, D. B., Ryan, S., Nash, J., Zhang, L., Maddox, P. S., Nedelec, F. and Maddox, A. S. (2018). Cross-linkers both drive and brake cytoskeletal remodeling and furrowing in cytokinesis. *Mol. Biol. Cell* **29**, 622–631.
- Dickinson, D. J., Robinson, D. N., Nelson, W. J. and Weis, W. I. (2012). α -catenin and IQGAP regulate myosin localization to control epithelial tube morphogenesis in Dictyostelium. *Dev. Cell* **23**, 533–546.
- Duan, R., Kim, J. H., Shilagardi, K., Schiffrhauer, E. S., Lee, D. M., Son, S., Li, S., Thomas, C., Luo, T., Fletcher, D. A. et al. (2018). Spectrin is a mechanoresponsive protein shaping fusogenic synapse architecture during myoblast fusion. *Nat. Cell Biol.* **20**, 688–698.
- Effler, J. C., Kee, Y.-S., Berk, J. M., Tran, M. N., Iglesias, P. A. and Robinson, D. N. (2006). Mitosis-specific mechanosensing and contractile protein redistribution control cell shape. *Curr. Biol.* **16**, 1962–1967.
- Egelhoff, T. T., Lee, R. J. and Spudich, J. A. (1993). Dictyostelium myosin heavy chain phosphorylation sites regulate myosin filament assembly and localization *in vivo*. *Cell* **75**, 363–371.
- Faix, J. and Weber, I. (2013). A dual role model for active Rac1 in cell migration. *Small GTPases* **4**, 110–115.
- Faix, J., Steinmetz, M., Boves, H., Kammerer, R. A., Lottspeich, F., Mintert, U., Murphy, J., Stock, A., Aebi, U. and Gerisch, G. (1996). Corticellins, major determinants of cell shape and size, are actin-bundling proteins with a parallel coiled-coil tail. *Cell* **86**, 631–642.
- Faix, J., Clougherty, C., Konzok, A., Mintert, U., Murphy, J., Albrecht, R., Muhlbauer, B. and Kuhlmann, J. (1998). The IQGAP-related protein DGAP1 interacts with Rac and is involved in the modulation of the F-actin cytoskeleton and control of cell motility. *J. Cell Sci.* **111**, 3059–3071.

- Faix, J., Weber, I., Mintert, U., Kohler, J., Lottspeich, F. and Marriott, G. (2001). Recruitment of cofilin into the cleavage furrow is controlled by Rac1 and IQGAP-related proteins. *EMBO J.* **20**, 3705–3715.
- Ferrell, J. E. Jr. (2013). Feedback loops and reciprocal regulation: recurring motifs in the systems biology of the cell cycle. *Curr. Opin. Cell Biol.* **25**, 676–686.
- Girard, K. D., Kuo, S. C. and Robinson, D. N. (2006). Dictyostelium myosin-II mechanochromism promotes active behavior of the cortex on long time-scales. *Proc. Natl. Acad. Sci. USA* **103**, 2103–2108.
- Hamann, J. C., Surcel, A., Chen, R., Teragawa, C., Albeck, J. G., Robinson, D. N. and Overholtzer, M. (2017). Entosis is induced by glucose starvation. *Cell Rep.* **20**, 201–210.
- Husbands, A. Y., Aggarwal, V., Ha, T. and Timmermans, M. C. P. (2016). In planta single-molecule pull-down reveals tetrameric stoichiometry of HD-ZIP1: LITTLE ZIPPER Complexes. *Plant Cell* **28**, 1783–1794.
- Jain, A., Liu, R., Ramani, B., Arauz, E., Ishitsuka, Y., Ragunathan, K., Park, J., Chen, J., Xiang, Y. K. and Ha, T. (2011). Probing cellular protein complexes using single-molecule pull-down. *Nature* **473**, 484–488.
- Kanada, M., Nagasaki, A. and Uyeda, T. Q. P. (2005). Adhesion-dependent and contractile ring-independent equatorial furrowing during cytokinesis in mammalian cells. *Mol. Biol. Cell* **16**, 3865–3872.
- Kee, Y.-S., Ren, Y., Dorfman, D., Iijima, M., Firtel, R., Iglesias, P. A. and Robinson, D. N. (2012). A mechanosensory system governs myosin II accumulation in dividing cells. *Mol. Biol. Cell* **23**, 1510–1523.
- Kim, J. H., Ren, Y., Ng, W. P., Li, S., Son, S., Kee, Y.-S., Zhang, S., Zhang, G., Fletcher, D. A., Robinson, D. N. et al. (2015). Mechanical tension drives cell membrane fusion. *Dev. Cell* **32**, 561–573.
- Kothari, P., Schiffhauer, E. S. and Robinson, D. N. (2017). Cytokinesis from nanometers to micrometers and microseconds to minutes. *Methods Cell Biol.* **137**, 307–322.
- Laplanche, C., Huang, F., Tebbis, I. R., Bewersdorf, J. and Pollard, T. D. (2016). Molecular organization of cytokinesis nodes and contractile rings by super-resolution fluorescence microscopy of live fission yeast. *Proc. Natl. Acad. Sci. USA* **113**, E5876–E5885.
- Laporte, D., Coffman, V. C., Lee, I.-J. and Wu, J.-Q. (2011). Assembly and architecture of precursor nodes during fission yeast cytokinesis. *J. Cell Biol.* **192**, 1005–1021.
- Lee, S., Shen, Z., Robinson, D. N., Briggs, S. and Firtel, R. A. (2010). Involvement of the cytoskeleton in controlling leading-edge function during chemotaxis. *Mol. Biol. Cell* **21**, 1810–1824.
- Luo, T. and Robinson, D. N. (2015). Kinetic Monte Carlo simulations of the assembly of filamentous biomacromolecules by dimer addition mechanism. *RSC Adv.* **5**, 3922–3929.
- Luo, T., Mohan, K., Srivastava, V., Ren, Y., Iglesias, P. A. and Robinson, D. N. (2012). Understanding the cooperative interaction between myosin II and actin crosslinkers mediated by actin filaments during mechanosensation. *Biophys. J.* **102**, 238–247.
- Luo, T., Mohan, K., Iglesias, P. A. and Robinson, D. N. (2013). Molecular mechanisms of cellular mechanosensing. *Nat. Mater.* **12**, 1064–1071.
- Manukyan, A., Ludwig, K., Sanchez-Manchinelly, S., Parsons, S. J. and Stukenberg, P. T. (2015). A complex of p190RhoGAP-A and anillin modulates RhoA-GTP and the cytokinetic furrow in human cells. *J. Cell Sci.* **128**, 50–60.
- Mondal, S., Burgute, B., Rieger, D., Muller, R., Rivero, F., Faix, J., Schleicher, M. and Noegel, A. A. (2010). Regulation of the actin cytoskeleton by an interaction of IQGAP related protein GAP4 with filamin and cofilin I. *PLoS ONE* **5**, e15440.
- Ngo, T., Miao, X., Robinson, D. N. and Zhou, Q. Q. (2016). An RNA-binding protein, RNP-1, protects microtubules from nocodazole and localizes to the leading edge during cytokinesis and cell migration in Dictyostelium cells. *Acta Pharmacol. Sin.* **37**, 1449–1457.
- Peltz, G., Spudich, J. A. and Parham, P. (1985). Monoclonal antibodies against seven sites on the head and tail of Dictyostelium myosin. *J. Cell Biol.* **100**, 1016–1023.
- Poirier, C. C., Ng, W. P., Robinson, D. N. and Iglesias, P. A. (2012). Deconvolution of the cellular force-generating subsystems that govern cytokinesis furrow ingression. *PLoS Comput. Biol.* **8**, e1002467.
- Reichl, E. M., Ren, Y., Morphew, M. K., Delannoy, M., Effler, J. C., Girard, K. D., Divi, S., Iglesias, P. A., Kuo, S. C. and Robinson, D. N. (2008). Interactions between myosin and actin crosslinkers control cytokinesis contractility dynamics and mechanics. *Curr. Biol.* **18**, 471–480.
- Ren, Y., Effler, J. C., Norstrom, M., Luo, T., Firtel, R. A., Iglesias, P. A., Rock, R. S. and Robinson, D. N. (2009). Mechanosensing through cooperative interactions between myosin II and the actin crosslinker cofilin I. *Curr. Biol.* **19**, 1421–1428.
- Ren, Y., West-Foyle, H., Surcel, A., Miller, C. and Robinson, D. N. (2014). Genetic suppression of a phosphomimic myosin II identifies system-level factors that promote myosin II cleavage furrow accumulation. *Mol. Biol. Cell* **25**, 4150–4165.
- Robinson, D. N. and Spudich, J. A. (2000). Dynacortin, a genetic link between equatorial contractility and global shape control discovered by library complementation of a dictyostelium discoideum cytokinesis mutant. *J. Cell Biol.* **150**, 823–838.
- Ruppel, K. M., Uyeda, T. Q. and Spudich, J. A. (1994). Role of highly conserved lysine 130 of myosin motor domain. In vivo and in vitro characterization of site specifically mutated myosin. *J. Biol. Chem.* **269**, 18773–18780.
- Schiffhauer, E. S., Luo, T., Mohan, K., Srivastava, V., Qian, X., Griffis, E. R., Iglesias, P. A. and Robinson, D. N. (2016). Mechanoaccumulative elements of the mammalian actin cytoskeleton. *Curr. Biol.* **26**, 1473–1479.
- Srivastava, V. and Robinson, D. N. (2015). Mechanical stress and network structure drive protein dynamics during cytokinesis. *Curr. Biol.* **25**, 663–670.
- Sun, Q., Luo, T., Ren, Y., Florey, O., Shirasawa, S., Sasazuki, T., Robinson, D. N. and Overholtzer, M. (2014). Competition between human cells by entosis. *Cell Res.* **24**, 1299–1310.
- Surcel, A., Ng, W. P., West-Foyle, H., Zhu, Q., Ren, Y., Avery, L. B., Krenc, A. K., Meyers, D. J., Rock, R. S., Anders, R. A. et al. (2015). Pharmacological activation of myosin II paralogs to correct cell mechanics defects. *Proc. Natl. Acad. Sci. USA* **112**, 1428–1433.
- Surcel, A., Schiffhauer, E. S., Thomas, D. G., Zhu, Q., DiNapoli, K., Herbig, M., Otto, O., Guck, J., Jaffee, E. M., Iglesias, P. et al. (2017). Harnessing the adaptive potential of mechanoresponsive proteins to overwhelm pancreatic cancer dissemination and invasion. *bioRxiv*. 190553.
- Umbarger, H. E. (1956). Evidence for a negative-feedback mechanism in the biosynthesis of isoleucine. *Science* **123**, 848.
- Weissbach, L., Bernards, A. and Herion, D. W. (1998). Binding of myosin essential light chain to the cytoskeleton-associated protein IQGAP1. *Biochem. Biophys. Res. Commun.* **251**, 269–276.
- West-Foyle, H., Kothari, P., Osborne, J. and Robinson, D. N. (2018). 14-3-3 proteins tune non-muscle myosin II assembly. *J. Biol. Chem.* **293**, 6751–6761.
- Zhang, W. and Robinson, D. N. (2005). Balance of actively generated contractile and resistive forces controls cytokinesis dynamics. *Proc. Natl. Acad. Sci. USA* **102**, 7186–7191.
- Zhou, Q., Kee, Y.-S., Poirier, C. C., Jelinek, C., Osborne, J., Divi, S., Surcel, A., Will, M. E., Eggert, U. S., Muller-Taubenberger, A. et al. (2010). 14-3-3 coordinates microtubules, Rac, and myosin II to control cell mechanics and cytokinesis. *Curr. Biol.* **20**, 1881–1889.

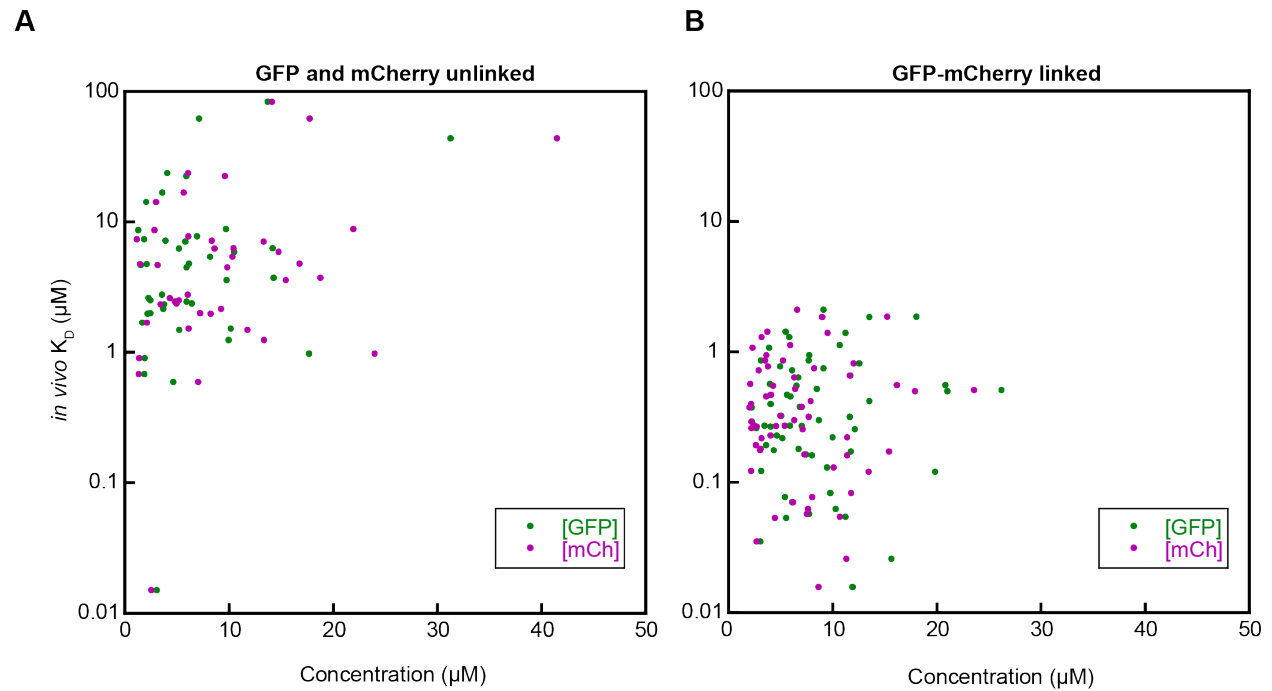


Figure S1. No correlation is detected between protein concentration and *in vivo* K_D . Plotting concentration of (A) GFP and mCherry unlinked or (B) linked in cells against *in vivo* K_D from FCCS shows no correlation.

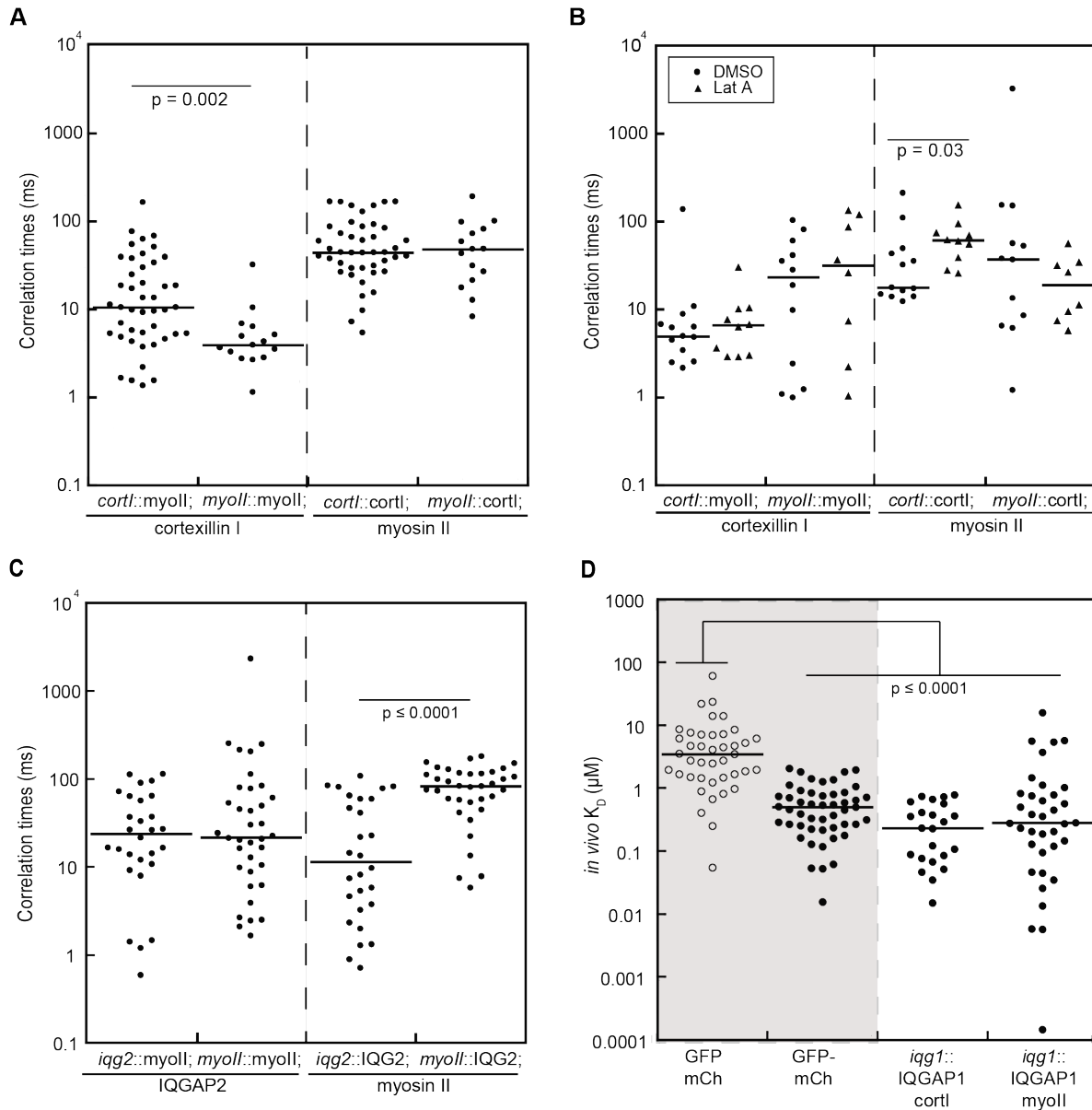


Figure S2. Correlation times of myosin II, cortexillin I, and IQGAP2, and *in vivo* K_D 's of IQGAP1 with myosin II and cortexillin I. (A) Correlation times measured for cortexillin I and myosin II in *cortl::myosin II*; cortexillin I and *myoll::myosin II*; cortexillin I cell lines. (B) Correlation times measured for cortexillin I and myosin II in same cell lines as (A), with and without Latrunculin A treatment. (C) Correlation times measured for IQGAP2 and myosin II in *iqg2::IQGAP2*; myosin II and *myoll::IQGAP2*; myosin II. (D) Shaded region indicates FCCS controls reproduced from Fig. 2B. IQGAP1 interacts with cortexillin I and myosin II by FCCS. Lines represent median values. P values are derived from Kruskal-Wallis followed by a Wilcoxon-Mann-Whitney test, comparing to the GFP and mCherry negative control. Negative and positive controls (shaded) are reproduced from Fig. 2B for side by side comparison. Open circles represent non-interactors.

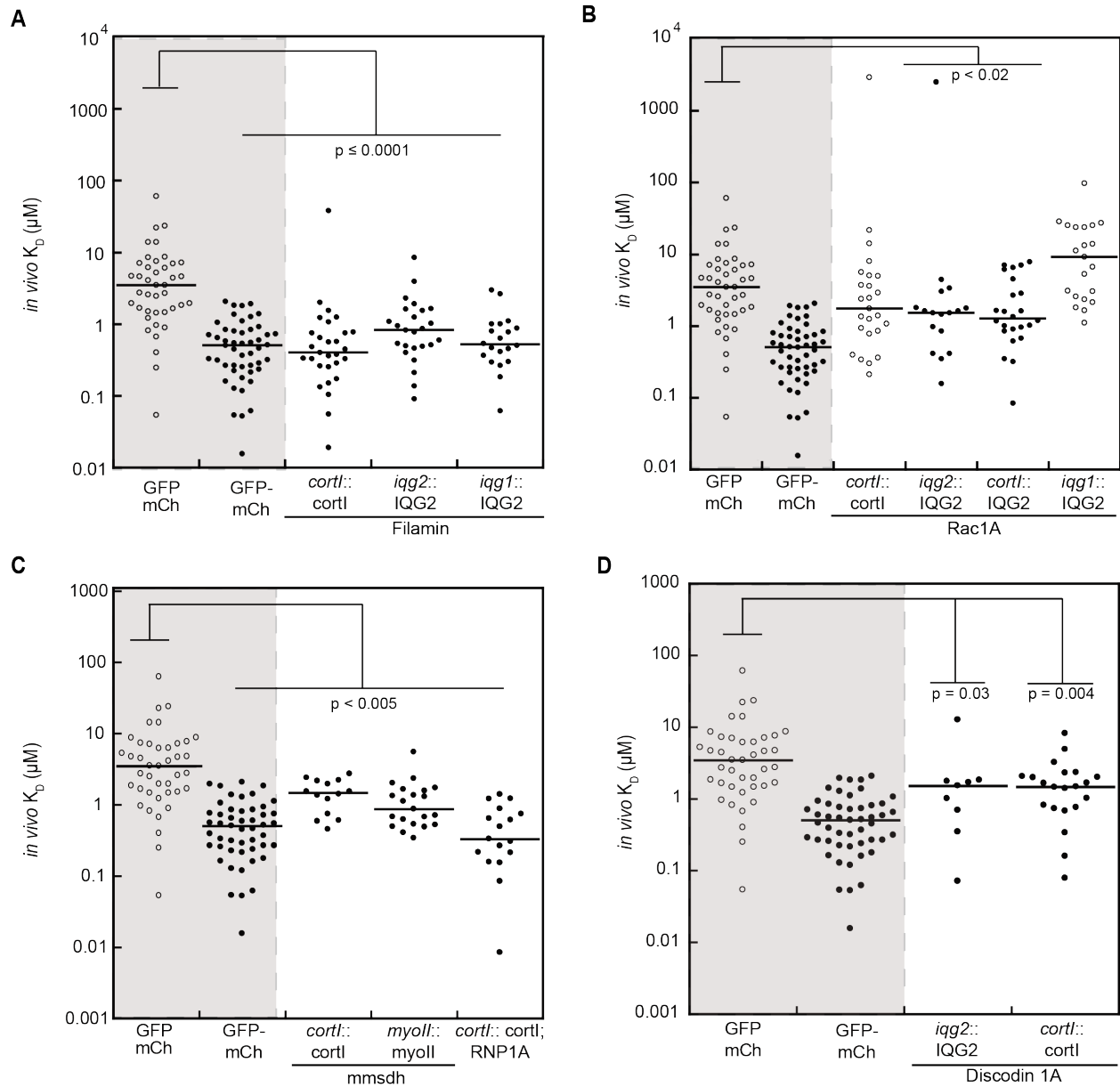


Figure S3. Apparent *in vivo* K_D 's measured for interactions from proteomics. Interactions measured by FCCS for cortexillin I, IQGAP2, or myosin II with (A) filamin, (B) Rac1A, (C) mmsdh and RNP1A, and (D) Discodien 1A in various genetic backgrounds. Lines represent median values. P values are derived from Kruskal-Wallis followed by a Wilcoxon-Mann-Whitney test, comparing to the GFP and mCherry negative control. Negative and positive controls (shaded) are reproduced from Fig. 2B for side by side comparison. Open circles represent non-interactors.

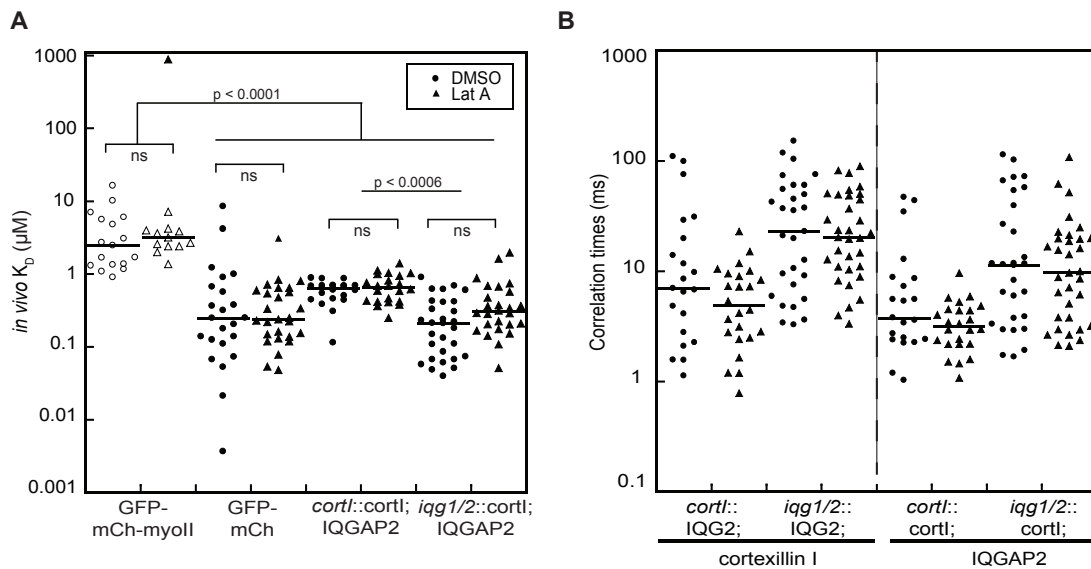


Figure S4. Interaction between IQGAP2 and cortexillin I is unaffected by Latrunculin A treatment. (A) Apparent *in vivo* K_D 's for negative control (GFP; mCh-myoll) and positive control (GFP-mCh) and cortexillin I and IQGAP2 in *cortl* null and *iqgap1/2* null strains under Latrunculin A treatment (5 μ M). The apparent binding affinity between IQGAP2 and cortexillin I still increases in the absence of IQGAP1. P values are derived from Kruskal-Wallis followed by a Wilcoxon-Mann-Whitney test, comparing to the GFP and mCherry negative control. Negative and positive controls are reproduced from **Fig. 2D** for side by side comparison. Open symbols indicate non-interactors. (B) Correlation times corresponding to (A) for cortexillin I and IQGAP2. No changes are detected with Latrunculin A treatment. Lines represent median values.

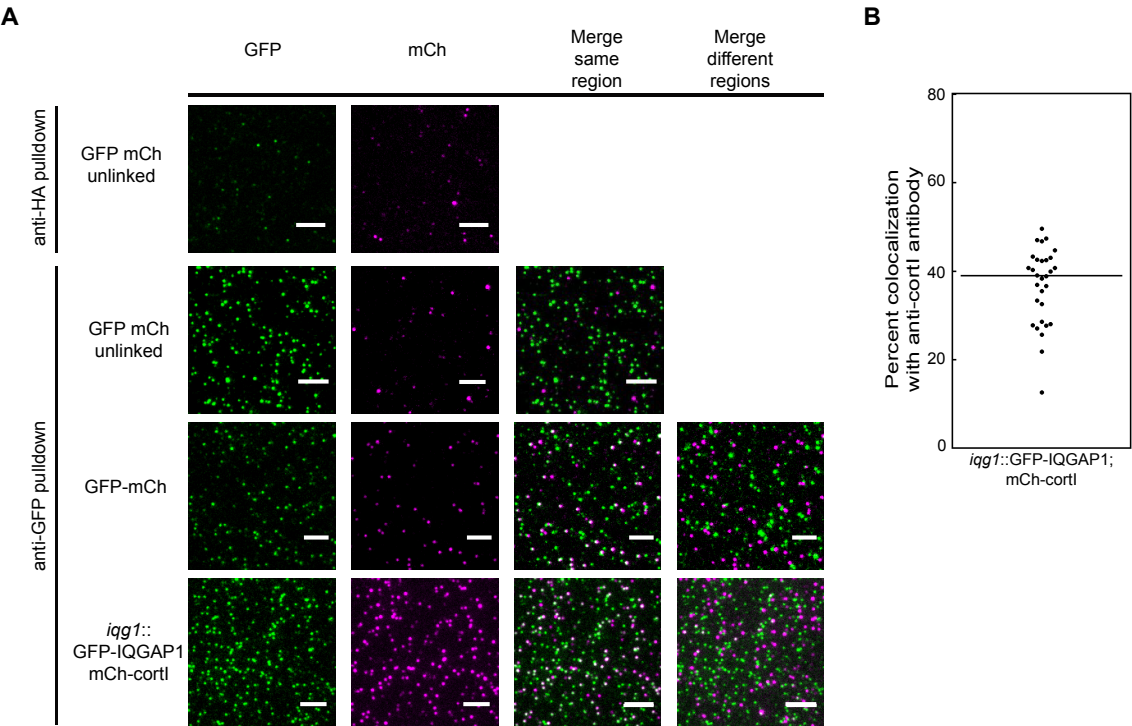


Figure S5. Single-molecule images demonstrate colocalization of cortexillin I with IQGAP1 and IQGAP2. (A) Representative single-molecule images for SiMPull of lysates with an anti-HA antibody to control for non-specific pull-down and the anti-GFP antibody. Columns show GFP, mCherry (no pulldown for GFP mCh unlinked), the corresponding merge images, and colocalization of images from different regions to measure random colocalization. Scale bar is 5 μ m. Each fluorescent spot is 8x8 pixels, and each pixel measures ~133 nm. **(B)** Cortexillin I colocalizes with IQGAP1 with anti-cortexillin-I antibody pull-down.

Table S1. Cortexillin I binding partners from mass spectrometry on cytosolic and cytoskeletal fractions of *cortI::FLAG-GFP-cortexillin I*. Normalized spectral counts and corresponding G-scores are listed.

Cytoskeletal Fraction		Counts		
Gene Name	Protein Name	GFP	CortI	G-score
<i>ctxA</i>	Cortexillin-I	0.0	16.5	22.8
<i>rgaA</i>	IQGAP1	0.0	16.4	22.7
<i>ctxB</i>	Cortexillin-II	0.0	13.4	18.5
<i>mhcA</i>	Myosin II heavy chain	2.3	12.1	7.3
<i>mfap1</i>	Protein MFAP1 homolog	0.0	4.9	6.8
<i>gapA</i>	IQGAP2	0.0	4.9	6.8
<i>DDB_0218327</i>	Putative uncharacterized protein	0.0	3.7	5.1
<i>DDB_0186471</i>	RNA-binding region RNP-1 domain-containing protein	0.0	3.4	4.8
<i>efbA</i>	Elongation factor 2	0.0	3.3	4.6
<i>rac1A</i>	Rho-related protein rac1A	0.0	3.3	4.6
<i>ndufa12</i>	NADH dehydrogenase[ubiquinone]1 alpha subcomplex subunit 12	0.0	3.0	4.1
<i>patB</i>	Probable plasma membrane ATPase	0.0	2.9	4.1
<i>mlcE</i>	Myosin essential light chain	0.0	2.6	3.6
Cytosolic Fraction				
Gene Name	Protein Name	GFP	CortI	G-score
<i>act22</i>	Putative actin-22	0.0	32.2	44.6
<i>DICPUDRAFT_90232</i>	Putative uncharacterized protein	0.0	29.1	40.3
<i>rgaA</i>	IQGAP1	0.0	25.6	35.5
<i>mhcA</i>	Myosin-2 heavy chain	2.0	31.8	31.5
<i>ctxA</i>	Cortexillin-I	0.0	22.3	30.9
<i>fkbp5</i>	FK506-binding protein 5	0.0	14.8	20.6
<i>ctxB</i>	Cortexillin-II	0.0	14.6	20.2
<i>cdcD</i>	Cell division cycle protein 48	26.3	65.5	17.3
<i>gapA</i>	IQGAP2	0.0	11.5	16.0
<i>ctr9</i>	RNA polymerase II complex component	0.0	9.6	13.4
<i>pyr1-3</i>	Protein PYR1-3	0.0	8.0	11.1
<i>efbA</i>	Elongation factor 2	0.0	6.7	9.3
<i>DICPUDRAFT_93127</i>	Putative uncharacterized protein	0.0	6.7	9.3
<i>DDB_0188474</i>	DUF814 family protein	0.0	6.1	8.4
<i>eef1a1</i>	Elongation factor 1-alpha	3.9	16.1	7.9
<i>rps3a</i>	40S ribosomal protein S3	1.4	10.3	7.6
<i>DDB_G0291301</i>	Putative bifunctional amineoxidase	0.0	5.5	7.6
<i>leo1</i>	RNA polymerase-associated protein	0.0	5.4	7.5
<i>acpB</i>	F-actin-capping protein subunit alpha	0.0	5.3	7.4
<i>paf1</i>	RNA polymerase II-associated factor 1	0.0	5.0	6.9
<i>ifdA</i>	DEAD/DEAH box helicase domain-containing protein	0.0	4.9	6.7
<i>tufm</i>	Elongation factor Tu, mitochondrial	0.0	4.8	6.6
<i>DDB_G0282483</i>	Uncharacterized transmembrane protein	0.0	4.4	6.1
<i>cdc73</i>	RNA polymerase II complex component	0.0	4.1	5.7
<i>acly</i>	Probable ATP-citrate synthase	0.0	4.0	5.5
<i>DDB_0169491</i>	Putative uncharacterized protein	0.0	4.0	5.5
<i>rpl13</i>	60S ribosomal protein L13	0.0	3.8	5.3
<i>DD8-14</i>	AAA ATPase domain-containing protein	0.0	3.8	5.2
<i>metK</i>	S-adenosyl methionine synthase	0.0	3.7	5.2

<i>rps23</i>	40S ribosomal protein S23	0.0	3.5	4.9
<i>DDB_G0277077</i>	UvrB/UvrC domain-containing protein	0.0	3.5	4.9
<i>DDB_0187217</i>	Putative uncharacterized protein	0.0	3.4	4.7
<i>mcfQ</i>	Mitochondrial substrate carrier family protein Q	0.0	3.3	4.6
<i>DICPUDRAFT_52099</i>	40S ribosomal protein S26	0.0	3.2	4.5
<i>abpC</i>	Gelation factor	0.0	3.2	4.4
<i>tubB</i>	Tubulin beta-chain	0.0	3.1	4.3
<i>rpl30</i>	60S ribosomal protein L30	3.2	10.7	4.3
<i>mmsdh</i>	Probable methylmalonate-semialdehyde dehydrogenase[acylating], mitochondrial	0.0	3.1	4.2
<i>wdr61</i>	WD repeat-containing protein61	0.0	3.1	4.2
<i>cyc1</i>	Cytochrome c1, heme protein, mitochondrial	0.0	3.1	4.2
<i>mcfZ</i>	Mitochondrial substrate carrier family protein Z	0.0	3.0	4.1
<i>rpl18</i>	60S ribosomal protein L18	0.0	3.0	4.1
<i>pdhC</i>	Dihydrolipoyllysine-residue acetyltransferase component of pyruvate dehydrogenase complex, mitochondrial	0.0	2.8	3.9
<i>DICPUDRAFT_48405</i>	Putative uncharacterized protein	0.0	2.7	3.7
<i>rac1A</i>	Rho-related protein rac1A	0.0	2.7	3.7
<i>odhB</i>	Dihydrolipoyllysine-residue succinyltransferase component of 2-oxoglutarate dehydrogenase complex, mitochondrial	0.0	2.7	3.7
<i>mlcE</i>	Myosin essential light chain	0.0	2.7	3.7

Table S2. IQGAP2 binding partners from mass spectrometry on cytosolic and cytoskeletal fractions of *iqg2::FLAG-GFP-IQGAP2*. Normalized spectral counts and corresponding G-scores are listed.

Cytoskeletal Fraction		Counts		
Gene Name	Protein Name	GFP	IQG2	G-score
<i>act1</i>	Major actin	0.0	27.3	37.91
<i>hspA</i>	60kDa heat shock protein, mitochondrial	4.7	24.1	14.40
<i>gapA</i>	IQGAP2	0.0	9.8	13.54
<i>act24</i>	Putative actin-24	0.0	8.8	12.19
<i>dscA</i>	Discoidin-1 subunit A	0.0	6.2	8.60
<i>ctxB</i>	Cortexillin-II	0.0	6.1	8.41
<i>ctxA</i>	Cortexillin-I	0.0	5.1	7.08
<i>act18</i>	Actin-18	0.0	4.8	6.66
<i>DDB_0218327</i>	Putative uncharacterized protein	0.0	4.4	6.16
<i>rpl12</i>	60S ribosomal protein L12	0.0	4.4	6.07
<i>mlcE</i>	Myosin essential light chain	0.0	3.5	4.81
<i>rplp2</i>	60S acidic ribosomal protein P2	7.9	17.8	3.94
<i>efbA</i>	Elongation factor 2	0.0	2.8	3.91
Cytosolic Fraction				
Gene Name	Protein Name	GFP	IQG2	G-score
<i>dscA</i>	Discoidin-1 subunit A	0.0	17.0	23.60
<i>mhcA</i>	Myosin-2 heavy chain	2.0	19.3	16.14
<i>gapA</i>	IQGAP2	0.0	9.9	13.66
<i>ctxB</i>	Cortexillin-II	0.0	8.0	11.07
<i>ctxA</i>	Cortexillin-I	0.0	7.6	10.49
<i>dcsC</i>	Discoidin-1 subunitB/C	7.2	24.8	10.31
<i>fkbp5</i>	FK506-binding protein 5	0.0	7.3	10.18
<i>leo1</i>	RNA polymerase-associated protein	0.0	6.4	8.85
<i>rplp2</i>	60S acidic ribosomal protein P2	8.3	22.0	6.45
<i>dscE</i>	Discoidin-2	4.6	15.6	6.38
<i>cadA</i>	Calcium-dependent cell adhesion molecule	0.0	4.0	5.55
<i>rplp1</i>	60S acidic ribosomal protein P1	1.4	8.1	5.27
<i>cdcD</i>	Cell division cycle protein 48	26.3	43.6	4.32
<i>acpB</i>	F-actin-capping protein subunit alpha	0.0	3.0	4.19
<i>DICPUDRAFT_74418</i>	Putative uncharacterized protein	0.0	2.9	4.01

Table S3. IQGAP2 binding partners from mass spectrometry on cytosolic and cytoskeletal fractions of *cortIII::FLAG-GFP-IQGAP2*. Normalized spectral counts and corresponding G-scores are listed.

Cytoskeletal Fraction		Counts		
Gene Name	Protein Name	GFP	IQG2	G-score
<i>act18</i>	Actin-18	0.0	3.3	4.61
<i>gapA</i>	IQGAP2	0.0	2.6	3.66
Cytosolic Fraction				
Gene Name	Protein Name	GFP	IQG2	G-score
<i>mhcA</i>	Myosin-2 heavy chain	2.0	66.1	76.13
<i>fkbp5</i>	FK506-binding protein 5	0.0	11.0	15.27
<i>leo1</i>	RNA polymerase-associated protein	0.0	5.7	7.84
<i>acpB</i>	F-actin-capping protein subunit alpha	0.0	5.4	7.55
<i>cdcD</i>	Cell division cycle protein 48	26.3	49.2	7.07
<i>ctr9</i>	RNA polymerase II complex component	0.0	4.6	6.40
<i>mlcE</i>	Myosin essential light chain	0.0	4.3	6.00
<i>gapA</i>	IQGAP2	0.0	4.3	5.95
<i>mcfZ</i>	Mitochondrial substrate carrier family protein Z	0.0	3.0	4.12

Table S4. Concentrations and *in vivo* K_D 's by FCCS.

Concentrations and *in vivo* K_D 's are presented. Top row in *italics* indicates genetic background for each parameter set. Concentrations of Cortexillin I, Myosin II, IQGAP1, and Filamin are in $\mu\text{M}_{\text{dimer}}$ (where in this case when we refer to the myosin II dimer, this is the hexamer with two heavy chains and four light chains, which constitutes the functional 'monomer') while concentrations of IQGAP2, Mmsdh, RNP1A, Rac1A, and Discoidin 1A are in $\mu\text{M}_{\text{monomer}}$. Concentrations were normally distributed in real space and are listed as mean \pm s.e.m. For *in vivo* K_D 's, values were broadly distributed and nearly log normal. Therefore, in the top row, the log-space median values are provided with real space transformed medians with units in μM included in the parentheses. The log-space mean \pm s.e.m. values are provided in the bottom row.

[Click here to Download Table S4](#)

Table S5. List of *Dictyostelium* strains used in this study.

Strain	Plasmids transformed
<i>cortl</i> :: FLAG-GFP-cortexillin I	FLAG-GFP-cortexillin I pDRH; pDM181
<i>cortl</i> :: FLAG-GFP	FLAG-GFP pDRH; pDM181
<i>iqg2</i> :: FLAG-GFP-IQGAP2	FLAG-GFP-IQGAP2 pDRH; pDM181
<i>iqg2</i> :: FLAG-GFP	FLAG-GFP pDRH; pDM181
<i>cortl/II</i> :: FLAG-GFP-IQGAP2	FLAG-GFP-IQGAP2 pDRH; pDM181
<i>cortl/II</i> :: FLAG-GFP	FLAG-GFP pDRH; pDM181
KAx3::FLAG-GFP	FLAG-GFP pDRH; pDM181
KAx3::GFP; mCherry	GFP pDM181; mCherry pDRH
KAx3::GFP-5aa-mCherry	GFP-5aa-mCherry pDM181; pDRH
<i>myoII</i> ::GFP-myosin-II; mCherry	GFP-myosin-II pBig; mCherry pDRH
<i>myoII</i> ::GFP-myosin S1-mCherry	GFP-myosin S1-mCherry pDM181
<i>myoII</i> ::GFP-myosin-II; mCherry-cortl	GFP-myosin-II pBig; mCherry-cortl pDRH
<i>myoII</i> ::GFP-IQGAP2; mCherry-myosin-II	GFP-IQGAP2 pExp4; mCherry-myosin-II pDRH
<i>myoII</i> ::GFP-myosin II; mCherry-IQGAP2	GFP-myosin II pBig; mCherry-IQGAP2 pDRH
<i>myoII</i> ::GFP-myosin II-3xAsp; mCherry-IQGAP2	GFP-myosin II-3xAsp pBig; mCherry-IQGAP2 pDRH
<i>myoII</i> :: GFP-IQGAP2; mCherry-cortl	GFP-IQGAP2 pExp4; mCherry-cortl pDRH
<i>cortl</i> :: GFP-IQGAP2; mCherry-cortl	GFP-IQGAP2 pExp4; mCherry-cortl pDRH
<i>cortl</i> :: GFP-myosin-II; mCherry-cortl	GFP-myosin-II pBig; mCherry-cortl pDRH
<i>cortl</i> :: GFP-IQGAP2; mCherry-myoII	GFP-IQGAP2 pExp4; mCherry-myosin-II pDRH
<i>iqg1</i> :: GFP-myosin-II; mCherry-cortl	GFP-myosin-II pBig; mCherry-cortl pDRH
<i>iqg1</i> :: GFP-IQGAP1; mCherry-cortl	GFP-IQGAP1 pExp4; mCherry-cortl pDRH
<i>iqg1</i> :: GFP-myosin-II; mCherry-IQGAP1	GFP-myosin-II pBig; mCherry-IQGAP1 pDRH
<i>iqg1</i> :: GFP-IQGAP2; mCherry-myosin-II	GFP-IQGAP2 pExp4; mCherry-myosin-II pDRH
<i>iqg2</i> :: GFP-myosin-II; mCherry-cortl	GFP-myosin-II pBig; mCherry-cortl pDRH
<i>iqg2</i> :: GFP-IQGAP2; mCherry-cortl	GFP-IQGAP2 pExp4; mCherry-cortl pDRH
<i>iqg2</i> :: GFP-IQGAP2; mCherry-myoII	GFP-IQGAP2 pExp4; mCherry-myosin-II pDRH
<i>iqg2</i> :: GFP-myoII; mCherry-IQGAP2	GFP-myosin II pBig; mCherry-IQGAP2 pDRH
<i>iqg1/2</i> :: GFP-IQGAP2; mCherry-cortl	GFP-IQGAP2 pExp4; mCherry-cortl pDRH
<i>iqg1/2</i> :: GFP-IQGAP2; mCherry-myosin-II	GFP-IQGAP2 pExp4; mCherry-myoII pDRH
<i>iqg1/2</i> :: GFP-myosin-II; mCherry-cortl	GFP-myosin-II pBig; mCherry-cortl pDRH
KAx3:: 14-3-3-GFP	14-3-3-GFP pLD1; pREP
<i>cortl</i> :: GFP-mmsdh; mCherry-cortl	GFP-mmsdh pDM181; mCherry-cortl pDRH
<i>myoII</i> :: GFP-mmsdh; mCherry-myosin-II	GFP-mmsdh pDM181; mCherry-myoII pDRH
<i>cortl</i> :: GFP-Rac1A; mCherry-cortl	GFP-Rac1A pDM181; mCherry-cortl pDRH
<i>cortl</i> :: GFP-RNP-1A; mCherry-cortl	GFP-RNP-1A pLD1; mCherry-cortl pDRH
<i>cortl</i> :: GFP-Filamin; mCherry-cortl	GFP-Filamin pDXA; mCherry-cortl pDRH
<i>cortl</i> :: GFP-Discoidin 1A; mCherry-cortl	GFP-Discoidin 1A pDM181; mCherry-cortl pDRH
<i>iqg2</i> :: GFP-Rac1A; mCherry-IQGAP2	GFP-Rac1A pDM181; mCherry-IQGAP2 pDRH
<i>iqg1</i> :: GFP-Rac1A; mCherry-IQGAP2	GFP-Rac1A pDM181; mCherry-IQGAP2 pDRH
<i>cortl</i> :: GFP-Rac1A; mCherry-IQGAP2	GFP-Rac1A pDM181; mCherry-IQGAP2 pDRH
<i>iqg2</i> :: GFP-Filamin; mCherry-IQGAP2	GFP-Filamin pDXA; mCherry-IQGAP2 pDRH
<i>iqg1</i> :: GFP-Filamin; mCherry-IQGAP2	GFP-Filamin pDXA; mCherry-IQGAP2 pDRH
<i>iqg2</i> :: GFP-Discoidin 1A; mCherry-IQGAP2	GFP-Discoidin 1A pDM181; mCherry-IQGAP2 pDRH